A Semi-Automatic Approach for Epicardial Adipose Tissue Segmentation and Quantification on Cardiac CT Scans

Carmelo Militello[1], Leonardo Rundo[2,3,1], Patrizia Toia[4], Vincenzo Conti[5], Giorgio Russo[1], Clarissa Filorizzo[4], Erica Maffei[6], Filippo Cademartiri[7], Ludovico La Grutta[8], Massimo Midiri[4], Salvatore Vitabile[4]

[1] Institute of Molecular Bioimaging and Physiology, Italian National Research Council (IBFM-CNR), Cefalù (PA), Italy

[2] University of Cambridge, Department of Radiology, Cambridge, United Kingdom

[3] Cancer Research UK Cambridge Centre, Cambridge, United Kingdom

[4] Department of Biomedicine, Neuroscience and Advanced Diagnostic (BiND), University of Palermo, Italy

[5] Faculty of Engineering and Architecture, University of Enna KORE, Enna, Italy

[6] Cardiovascular Imaging Unit, SDN Foundation IRCCS, Naples, Italy

[7] Department of Radiology, Area Vasta 1/ASUR Marche, Urbino, Italy

[8] Department of Health Promotion Sciences Maternal and Infantile Care, Internal Medicine and Medical Specialities (ProMISE), University of Palermo, Italy

Abstract. Many studies have shown that epicardial fat is associated with a higher risk of heart diseases. Accurate epicardial adipose tissue quantification is still an open research issue. Considering that manual approaches are generally user-dependent and time-consuming, computer-assisted tools can considerably improve the result repeatability as well as reduce the time required for performing an accurate segmentation. Unfortunately, fully automatic strategies might not always identify the Region of Interest (ROI) correctly. Moreover, they could require user interaction for handling unexpected events.

This paper proposes a semi-automatic method for Epicardial Fat Volume (EFV) segmentation and quantification. Unlike supervised Machine Learning approaches, the method does not require any initial training or modeling phase to set up the system. As a further key novelty, the method also yields a subdivision into quartiles of the adipose tissue density. Quartile-based analysis conveys information about fat densities distribution, enabling an in-depth study towards a possible correlation between fat amounts, fat distribution, and heart diseases.

Experimental tests were performed on 50 of Calcium Score (CaSc) series and 95 of Coronary Computed Tomography Angiography (CorCTA) series. Area-based and distance-based metrics were used to evaluate the segmentation accuracy, by obtaining Dice Similarity Coefficient (DSC)=93.74% and Mean Absolute Distance (MAD)=2.18 for CaSc, as well as DSC=92.48% and MAD=2.87 for CorCTA. Moreover, the Pearson and Spearman coefficients were computed for quantifying the correlation between the ground-truth EFV and the corresponding automated measurement, by obtaining 0.9591 and 0.9490 for CaSc, and 0.9513 and 0.9319 for CorCTA, respectively.

In conclusion, the proposed EFV quantification and analysis method represents a clinically usable tool assisting the cardiologist to gain insights into a specific clinical scenario and leading towards personalized diagnosis and therapy.

Keywords: *epicardial fat volume; cardiac adipose tissue quantification; semi-automatic segmentation; calcium score scans; coronary computed tomography angiography scans; fat density quartiles.*

1. Introduction

Cardiovascular diseases are characterized by a multifactorial etiology and several factors may contribute simultaneously to their development. The conditions that cause an increase in the probability of the disease onset are called "risk factors"; they are subdivided into modifiable, *via* lifestyle changes or drugs (e.g., arterial hypertension, life habits, diabetes mellitus, hypercholesterolemia), and not modifiable (e.g., age, sex, and genetic background) [1][2][3][4][5]. Considering this situation, studying the modifiable risk factors is relevant for defining targeted therapies.

Over the last decades, experimental findings report a growing interest in the study of adipose tissue, by indicating a strong correlation between the risk of future heart disease and the volume of adipose tissue inside of the pericardium. Indeed, this tissue represents a valuable predictor of cardio- and cerebro-vascular events, regardless of other risk factors [6][7].

In particular, even more interest was devoted to the analysis and quantification of the epicardial fat tissue, which surrounds the whole heart as well as the coronary, and it is generally characterized by an inhomogeneous appereance. These differences are mainly due to different fat densities, but also to artifacts/errors of tomographic reconstruction algorithms [8][9]. Among the diagnostic imaging modalities, Computed Tomography (CT) [10][11][12][13][14][15] and Magnetic Resonance Imaging (MRI) [16][17][18] represent both valid techniques for adipose tissue imaging. During the latest years, the most validated, and reproducible quantification is obtained by using CT. Moreover, in addition to lower costs with respect to MRI, an additional reason endorsing a greater diffusion of the CT is the difficulty associated to the localization of the pericardium in cardiovascular MR images. As a matter of fact, the pericardium is usually difficult to detect on MRI (i.e., it is hardly visible as a very thin line, typically blurred due to partial volume effects).

Nowadays, manual procedures for Epicardial Fat Volume (EFV) segmentation and quantification are still diffused in the clinical practice. Manual approaches are user-dependent, due to the difficulty of correctly identifying the area among multiple observers. The time needed for reporting each individual patient has to be also taken into account. Therefore, computer-assisted tools, which are able to cope with these problems, are essential to improve the repeatability of results as well as to reduce the processing time.

Among automatic methodologies, atlas-based models are the most widely used solution in the literature. Undoubtedly, the atlases represent an excellent approach when the goal is the automatic identification of a Region of Interest (ROI) [19]. However, several issues must be considered in the case of atlas-based techniques [20][21]. A typical drawback could concern the intrinsic ambiguity arising in the atlas construction. Moreover, the performance of an atlas-based segmentation algorithm depends heavily on the registration step: if an atlas is poorly co-registered, the fusion step could misguide the segmentation of the target image, so decreasing its accuracy [20]. Nowadays, Machine Learning includes a set of advanced techniques that are obtaining excellent results, by strongly relying on high quality annotated large-scale datasets to be used in the training phase. In

[22], the authors proposed a fully-automatic approach based on a Convolutional Neural Network (CNN) [23] for the segmentation of the left atrium of the heart, by processing 3D late gadolinium-enhanced MRI series. This approach might be certainly relevant, even though the aims are very different from ours, mainly because the challeges regarding cardiac MR images analysis considerably differ from CT-based tissue density measurements.

Moreover, several literature works showed that morphology of human organs, like the brain, is highly variable among phenotypically different ethnic groups with fundamental genetic and environmental variations in brain morphology and microstructure (e.g., shape, size and volume) [24][25]. Also, it is necessary to consider that used atlas are rather static, since they do not capture the subjects' characteristics as a function of age and gender [26]. However, these brain atlases have been not yet ready for practical applications due to some deficiencies, particularly arising in multi-centric studies [21]. In general, this rationale may be extended to any human organ. Thus, atlas-based approaches have limitations, especially in those scenarios where higher variability of morphology is expected.

Starting from a well-established question from chest radiologists, the clinical rationale and feasibility have always been taken into account in the design choices. This led to a solution based on a semi-automatic strategy that allows for a safe end-user control of the automated result, providing reliable and validated (by an expert radiologist) results. Our computational solution, which does not require any training phase, considerably facilitates the direct translation and deployment of the approach into the clinical practice [27].

Considering these premises, the objective of this study is to provide an approach allowing us to support the clinician workflow: the availability of a computer-assisted tool, which can enable the EFV identification and support the screening/follow-up protocols of patients' categories with cardiovascular risk factors, makes it possible to reduce some typical drawbacks of manual segmentation procedures. The EFV quantification – for instance, before and after the administration of drug therapy with statins – could help the cardiologist to provide useful indications to modify an inappropriate 'lifestyle' and, more importantly, improve the drug treatment with targeted interventions. However, it is worth considering that in clinical contexts, fully automatic solutions might not be always suitable, because the human intervention is often required in the reporting phase. This fact motivated us to develop a semi-automatic approach to assist clinicians in the EFV quantification procedure. Our computer-assisted approach detects and quantifies the EFV, by allowing the cardiologist to interact and check the results during the initial phase. Moreover, our design choice overcomes some typical limitations of the automatic approaches that, needing for *a priori* knowledge for the training phase, are not always clinically feasible in the case of a small amount of enrolled subjects.

Research challenges. The main challenges on this research topics are:

- hurdles related to the applicability of supervised Machine Learning techniques and model-based approaches (i.e., atlases) in the clinical practice, due to the heterogeneity inherently characterizing patient scenarios;

- the conventional manual EFV quantification procedures strongly affect the result repeatability during patient follow-up visits.

Contributions. Our main contributions are:

- interactive support for the heart Volume of Interest (VOI) identification, remarkably alleviating the workload required by the clinician during the slice-by-slice EFV quantification;
- epicardial fat quartiles calculation for precision medicine purposes for gaining insights into the possible pathological scenarios;
- immediate feasibility and deployment in the clinical practice, introducing an approach that does not require neither training nor model setup phases [27].

Essentially, we propose here an appropriate and efficient combination of conventional methods and new approaches (particularly, in the interpolation step) tailored to deal with the problem of epicardial fat segmentation.

The paper is organized as follows: Section 2 reviews the related literature works addressing this issue; Section 3 presents the proposed semi-automatic approach for the EFV segmentation and quantification; Section 4 reports the achieved experimental results; Section 5 provides some discussions and comparisons with respect to state-of-the-art approaches; finally, conclusions and future directions are given in Section 5.

2. Related Works

Automated EFV analysis and quantification represent an interesting research topic, and the literature solutions refer to manual, automatic, and semi-automatic approaches. The majority of these methods analyzes CT images, since CT has a higher resolution allowing for precise detail identification with respect to MRI [28][29]. Moreover, the different densities of the analyzed tissues are natively and easily acquired by means of CT imaging: in our specific clinical scenario, CT allows us to identify epicardial fat and distinguish among density differences. Generally, CT imaging is used in the assessment of cardiovascular and coronary risks, while MRI allows for investigating the cardiac functionality [28][29]. The most relevant studies on EFV segmentation are outlined in what follows.

In [15] a semi-automatic method was implemented to firstly evaluate the epicardial fat volume and, successively, analyze the inter-observer variability. The method is based on a spherical harmonic representation of the epicardial surface applied non-contrast cardiac CT (NCT) for coronary calcium scan and Coronary CT Angiography (CorCTA). Two operators outlined the pericardial contours in Multi-Planar Reconstruction (MPR) visualizations (in order to obtain 2- and 4-chamber heart views) and in short axis views (by manually placing ROIs on 3 or 6 short-axis slices). The purpose of this work was to evaluate inter-observer variability of fat volume quantification rather than validating the proposed semi-automatic method.

In [30] a fully automatic approach for pericardium segmentation and epicardial fat volume estimation on CTA was presented, by exploiting a variant of multi-atlas segmentation and a random forest classifier for spatial initialization and accurate pericardium detection, respectively.

A method for autonomous segmentation and quantification of the epicardial and mediastinal cardiac fats was proposed in [31]. This methodology, aiming at minimizing user intervention, mainly comprises registration and classification algorithms to perform the desired segmentation. After the initial registration step, twenty patients (overall 878 images) were randomly chosen to compose a ground truth of cardiac fat. Successively, the features are extracted and provided as input to che classifier. The random forest algorithm outperfomed all the tested classifiers. After the cardiac fat area extraction, the volume is computed.

In [32] an automatic multi-atlas based method for segmenting the pericardium and calculating the EFV was developed. The data were acquired using two different scanners. Eight previously acquired CTA scans from different subjects were included as the atlas scans. The automatically segmented pericardium ROI is used to quantify the adipose tissue voxels, by appliyng a thresholding window in the Hounsfield Unit (HU) range [-200, …, -30].

In [35] the authors proposed a semi-automatic approach for segmentation and quantification of epicardial fat from 3D CT images. The method is a semi-automated slice-by-slice segmentation approach based on local adaptive morphology (i.e., a geometric ellipse for filtering out undesired parts of the target cluster) and fuzzy c-means clustering [36].

In [37] an alternative semi-automatic method for the analysis of CT images, obtained by the standard acquisition protocol used for coronary Calcium Score (CaSc), was proposed. Before the computerized processing phase, an expert observer has to scroll the slices between the atrioventricular sulcus and the apex in order to place some control points on the pericardium. Such control points are used to automatically draw a cubic spline on each slice, which represents the closed pericardium contour. This method is characterized by a two-step segmentation algorithm that is well-suited for the EFV quantification. In the first step, an analysis of epicardial fat intensity distribution is carried out to define suitable HU thresholds for a first rough segmentation. In the second step, a variational formulation of level set methods is used to recover spatial coherence and smoothness of fat depots.

Finally, with reference to Magnetic Resonance Angiography (MRA), an automatic approach for the segmentation of Pericardial Fat Volume (PFV) was proposed in [16]. Firstly, a rough segmentation of the heart region on the original image is performed by means of an atlas-based segmentation. To obtain the exact boundaries of the pericardial fat, a 3D graph-based segmentation is used to separate fatty and non-fatty components on the fat-only image.

These literature studies, where manual and automated tools to quantify pericardial fat are described, demonstrate that epicardial fat quantification is still an open research issue. Manual EFV quantification is not only a tedious and time consuming task, but more importantly the EFV is not easily identifable because of the

different densities. On the other hand, fully automated approaches could require either training phases, such as in the case of [16][30][31][32], or the use of ROI models before having a usable system. In clinical environments, especially when multi-institutional datasets are involved, designing and defining a reliable supervised model often requires specific solutions for achieving good generalization abilities [38][39].

Regardless of the adopted solution and the type of input images, the metodology should support the clinicians' activities by reducing the time required for analysis and reporting but, more importantly, must provide accurate and reliable results. Even though fully automatic approaches [16][30][31][32] do not need for the user intervention, semi-automatic methods [15][35][37], by involving an interactive input in at least one step of the processing pipeline, allow for safer results in critical domains. Therefore, considering the unique challenges encountered in clinical scenarios, interactive segmentation algorithms [40][41] often represent the safest and most feasible solution for physicians in clinical practice with respect to fully automatic approaches [42]. The proposed semi-automatic approach (described in Section 3) has the advantage of considerably improving the manual procedure, requiring the user interaction only in the first step of the processing pipeline. An exhaustive and structured comparison between the proposed approach and the state-of-the-art techniques is provided in Section 5, aiming at pointing out the main characteristics of each method, as well as the advantages and limitations when deployed in a clinical environment.

3. The Proposed Semi-Automatic Approach

As known from the pathological anatomy, the epicardial adipose tissue does not have a homogeneous distribution, and consequently its direct delineation is not feasible by means of manual procedures. As a matter of fact, manual approaches for the identification and segmentation of a specific ROI, such as the adipose tissue, would require a considerable amount of time for the radiologist and do not guarantee the result repeatability. In order to minimize the operator dependence on measurements and, consequently, improve the result repeatability, a computer-assisted procedure was designed and developed, allowing us to effectively improve the epicardial adipose tissue quantification by means of a semi-automatic method.

Our approach was used to implement a tool, providing also a user-friendly Graphical User Interface (GUI), able to support the radiologists in the procedure of EFV segmentation and quantification. In fact, taking a cardiac CT series as input, the tool – with few simple steps and with operator intervention only in the initial phase – yields the EFV and automatically performs the quantification of the fat quartiles and their distribution around the heart. As shown in Figure 1, the whole processing pipeline for the EFV segmentation and quantification can be divided into 4 mandatory steps and 2 optional steps: (*i*) ROI Selection; (*ii*) ROI Interpolation; (*iii*) ROI Refinement; (*iv*) Epicardial Adipose Tissue Segmentation; (*v*) Fat Volume and Quartiles Computation; (*vi*) Fat Thickness Measurement. The main processing pipeline and the optional operations are denoted by solid and dashed black lines, respectively. For better visualization purposes, the intermediate and final outputs of the main processing blocks are shown in Figure 2.

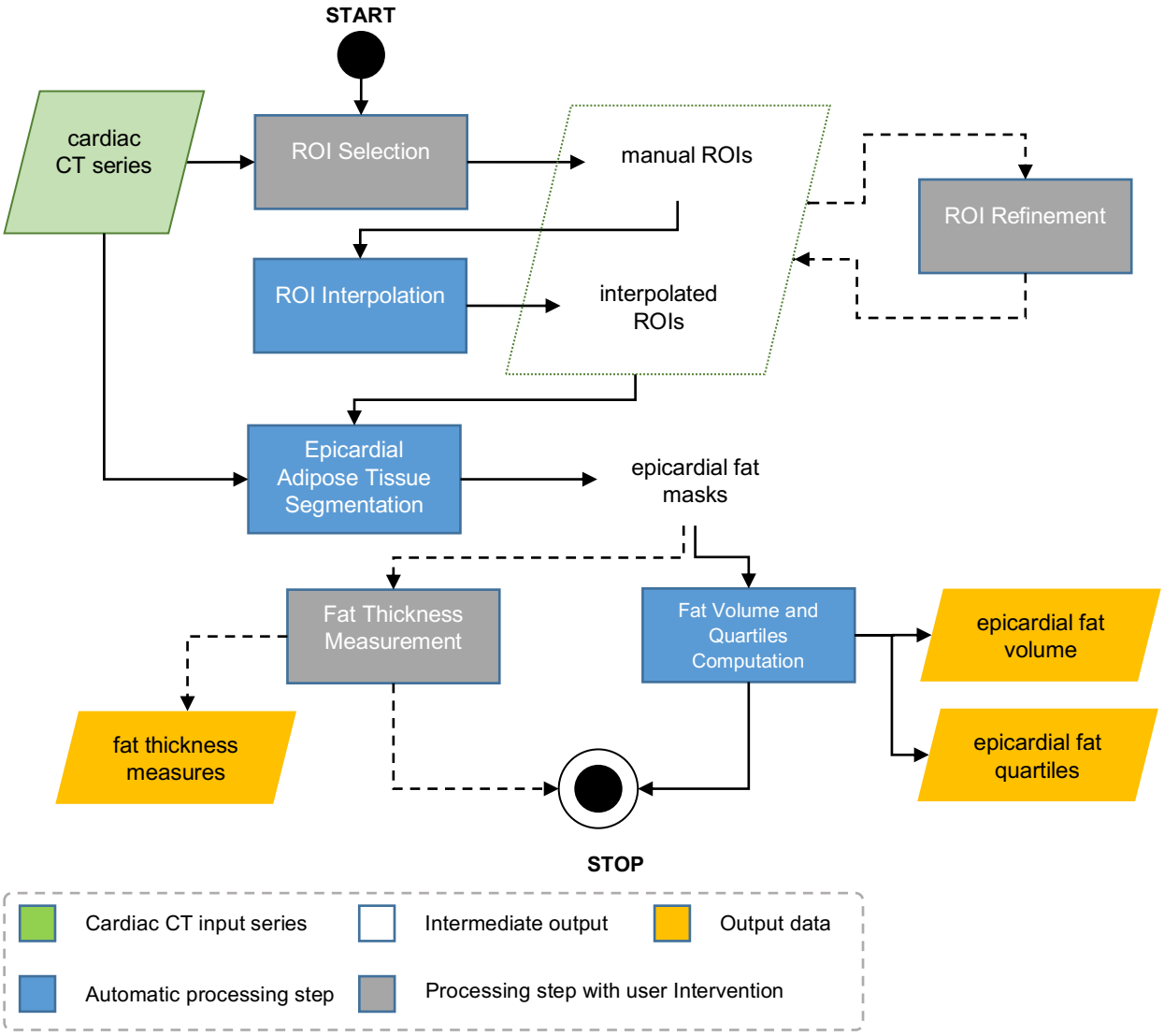

Figure 1. Overall flow diagram of the proposed semi-automatic approach for epicardial adipose tissue segmentation and quantification. The main processing pipeline and the optional operations are denoted by solid and dashed black lines, respectively. The notation used for the processing blocks is shown in the legend box.

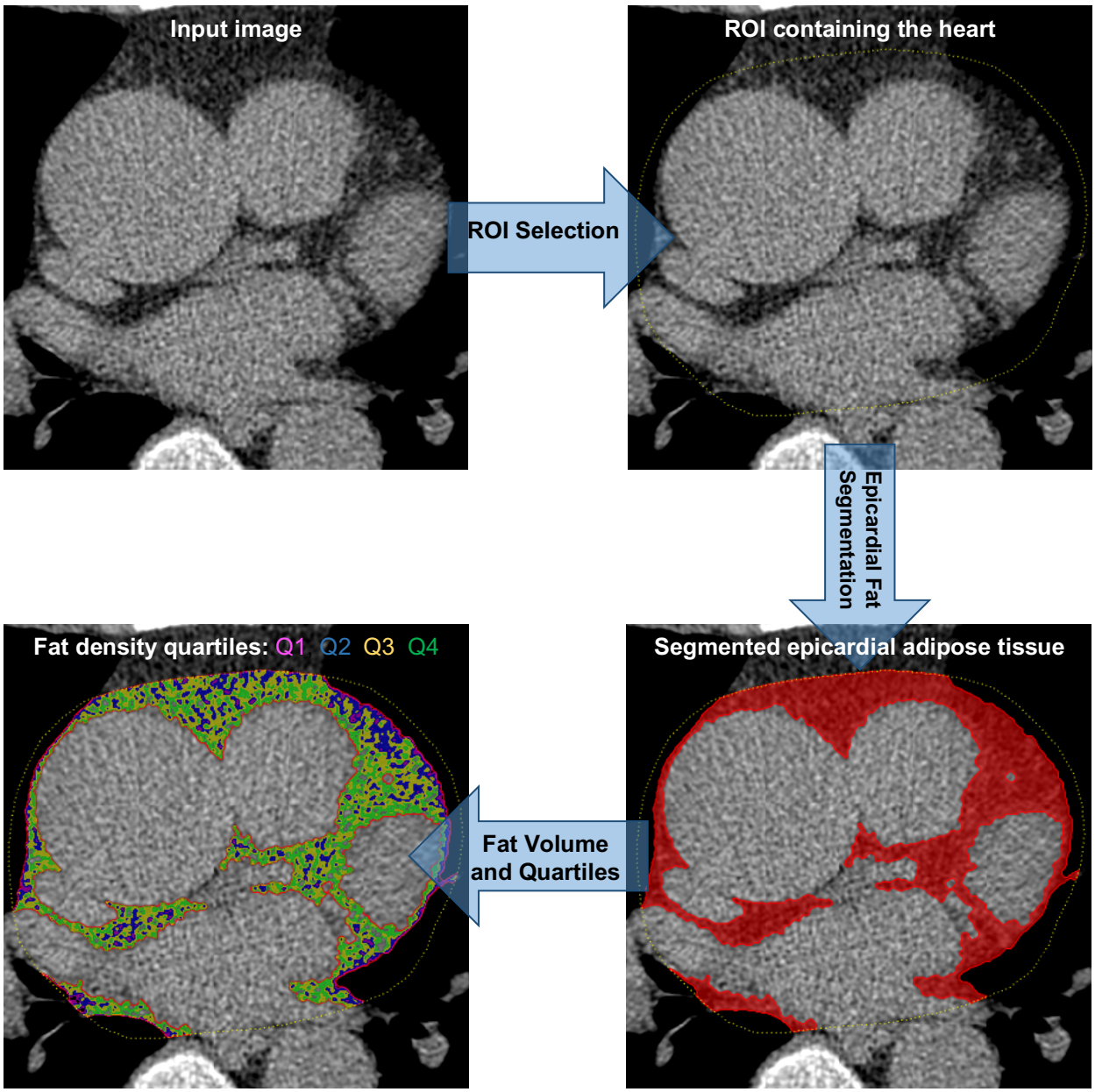

Figure 2. Workflow showing the main processing steps on an example CT cardiac image along with the corresponding intermediate outputs: *i*) initial input image; *ii*) ROI selection output; *iii*) epicardial adipose tissue segmentation; *iv*) fat volume and quartiles computation.

The proposed approach was entirely developed using the MatLab® R2016b environment (The MathWorks, Natick, MA, USA) and the implemented tool have been tested on a Microsoft® Windows 10 x64 platform, equipped with an Intel® i7@2.4GHz CPU and 8 GB of RAM. Each single processing step is described in detail in what follows. Figure 3 depicts the GUI of the implemented tool, exploiting the developed computational approach.

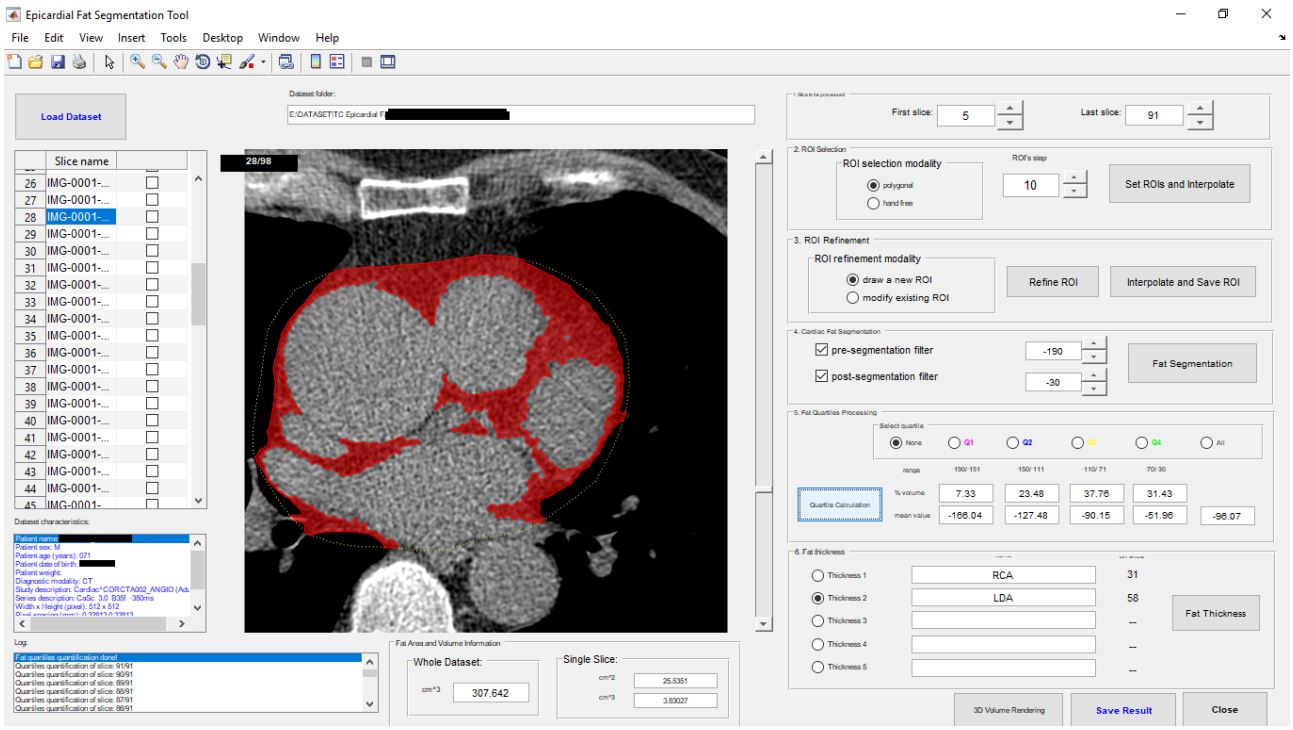

Figure 3. The GUI of the implemented tool for the EFV segmentation and quantification. On the left side, the list of all the slices belonging to the loaded CT series is displayed. In the central area, the selected image is displayed by over-imposing (transparency obtained by using alpha blending) the result of the performed segmented EFV. On the right side, the controls necessary to perform the various processing steps are shown.

3.1. ROI Selection

First of all, after selecting and loading the cardiac CT series, the operator must detect the bounding region containing the heart. Since it is not needed to process the whole series, but only the slices including the heart, the next step involves the specification of the slices range to analyze (by means of the parameters '*first_slice*' and '*last_sstlice*'). The analyzed CT series are cardiac CT CaSc and CorCTA. '*ROI_step*' is a parameter that indicates the offset between the slices wherein the ROI must be entered manually. Relying on physicians' indications, '*ROI_step*' default value was set to 10 and 20 for CaSc and CorCTA, respectively (by taking into account the *Slice thickness* parameter of the two datasets which, as reported in Table 1, is of 1.5 mm for CaSc and 0.75mm for CorCTA). In any case, the operator, when necessary, can modify the value of '*ROI_step*'. In our experimental trials the default values have always been used. Moreover, to ensure the best display mode, native windowing is automatically applied according to the values of the tags *window_center* and *window_width* retrieved from the DICOM header of the CT series. Figure 4 schematizes the strategy implemented to draw an ROI every *ROI_step* slices. Moreover, relying on the indications received from clinicians, we implemented two ROI tracing strategies: free-hand and polygonal lasso.

As shown in Table 1, the workload for the operator to set manually the reference ROIs is absolutely not excessive, having to set approximately 6 and 12 ROIs for the CaSc and CorCTA datasets, respectively.

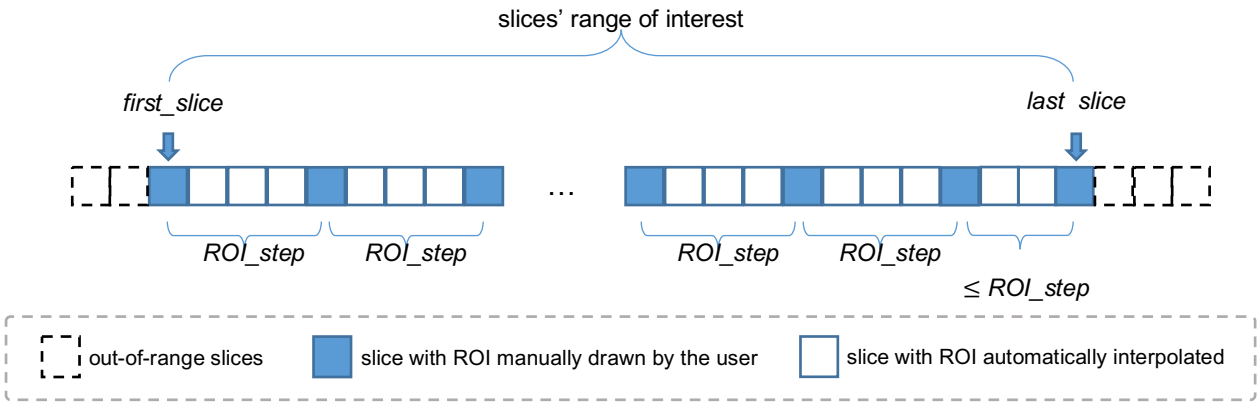

Figure 4. ROI detection is performed by considering only the slices' range of interest: starting from *'first_slice'*, just the slices every *'ROI_step'* offset are displayed (blue squares) in order to manually draw the ROI containing the heart. After inserting all the ROIs, until *'last_slice'* is reached, the ROI are interpolated onto the remaining slices included in the range of interest (white squares).

Considering that X and Y are the dimensions of the image (square images then $X = Y$), for every manually drawn ROI :

- $Centroid_{ROI_i} = (xc_i, yc_i)$ are the coordinates of the ith ROI centroid;
- $Points_{Circle} = \{(xc_j, yc_j) | j = 1, .., N_{points}\}$ is the set of coordinates of the N_{points} equi-spaced points on the circumscribed circumference with center $(X/2, Y/2)$ and radius $(X/2)\sqrt{2}$ (circumference circumscribed to the image);

As shown in Figure 5, for each manually drawn ROI, in order to perform the interpolation (next step), the N_{points} intersections between the ROI contour and the N_{points} straight lines – by joining the centroid $Centroid_{ROI_i}$ of the ith ROI and the 48 points on the circumference circumscribed to the image (belonging to the $Points_{Circle}$ set) – are determined. Experimentally, we set $N_{points} = 48$, as a compromise between (*i*) the accuracy in correctly following the ROI contour and (*ii*) limiting the computational complexity of the interpolation step.

$$Points_{ROI_i} = \{(xROI_{i,n}, yROI_{i,n}) \mid n = 1, \dots, N_{points}\}$$
$$\forall i \in [first\_slice, last\_slice] \wedge (\mathrm{mod}(i - first\_slice, ROI\_step) = 0). \quad (1)$$

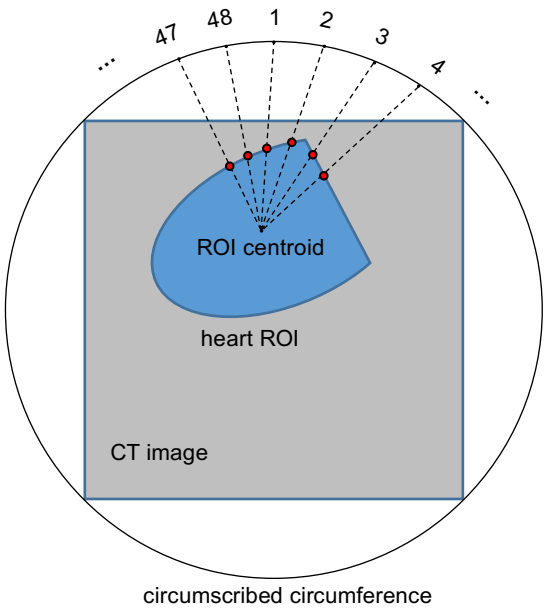

Figure 5. For each manually drawn ROI, in order to perform the interpolation, the 48 intersections between the ROI contour and the 48 straight lines – joining the centroid $Centroid_{ROI_i}$ of the ith ROI and the 48 points on the circumference circumscribed to the image (belonging to the $Points_{Circle}$ set) – are determined. The gray box and the blue-colored region represent the cardiac CT image and the heart ROI, respectively. The red dots denote the intersection points.

3.2. ROI Interpolation

Once the reference ROIs are manually drawn, the computational system automatically interpolates the ROIs in the remaining slices included in the range of interest. Especially, relying on these manual ROIs (traced every *'ROI_step'* slices), all the ROIs for the intermediate slices are computed by interpolating the ROIs drawn onto the slices '*i*' and '*i+ROI_step*' (see Figure 6). By so doing, the number of slices manually drawn by the user is reduced by a *'ROI_step'* factor.

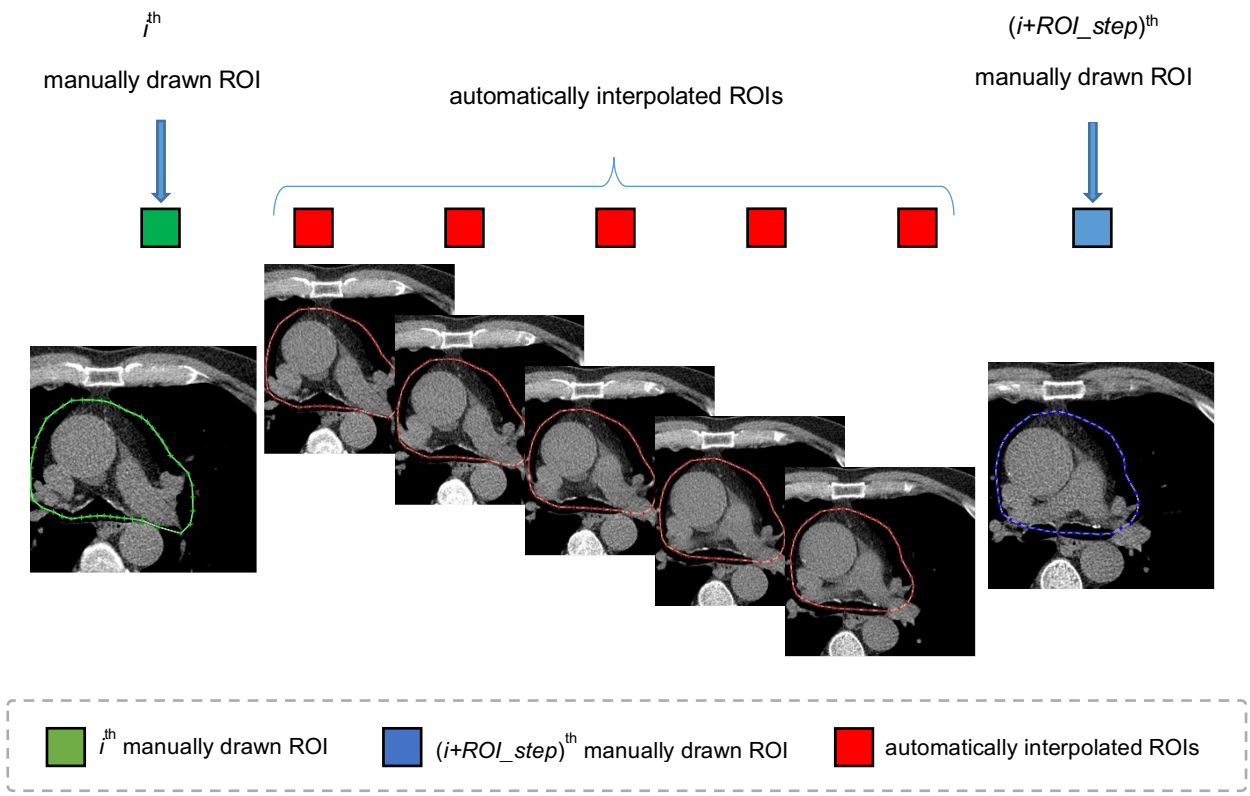

Figure 6. Example of interpolation of two reference ROIs. After manually drawing these two ROIs (denoted in green and blue, respectively), the remaining ROIs are automatically interpolated. In this case, to avoid displaying too many slices, *'ROI_step'* is set to 6 (implying 5 ROIs to be interpolated).

Considering the intersection points sets of i and $i + ROI\_step$ slices ($Points_{ROI_i}$ and $Points_{ROI_{i+ROI\_step}}$, respectively), defined by Eq. (1), it is possible to calculate the set $Points_{ROI_j}$ of the points of the jth interpolated ROI as:

$$Points_{ROI_j} = \{(xROI_{i,n} + j \cdot gapX_n, yROI_{i,n} + j \cdot gapY_n) \mid n = 1, \dots, N_{points}\},$$
$$\forall i \in [first\_slice, last\_slice] \wedge (mod(i - first\_slice, ROI\_step) = 0)$$
$$\forall j \in (i, i + ROI\_step). \tag{2}$$

As illustrated in Figure 7, $gapX_n$ and $gapY_n$ – defined by Eqs. (3) and (4), respectively – represent the distances along the x and y directions for the n_{th} point of the ROI that must be added j times to obtain the points interpolating the point pairs $(xROI_{i,n}, yROI_{i,n})$ and $(xROI_{i+ROI\_step,n}, yROI_{i+ROI\_step,n})$. This allows us to calculate the $ROI_{step} - 1$ missing ROIs.

$$gapX_n = (xROI_{i+ROI\_step,n} - xROI_{i.n})/(ROI\_step - 1), \forall n = 1, \dots, N_{points} \tag{3}$$

$$gapY_n = (yROI_{i+ROI\_step,n} - yROI_{i,n})/(ROI\_step - 1), \forall n = 1, \dots, N_{points} \tag{4}$$

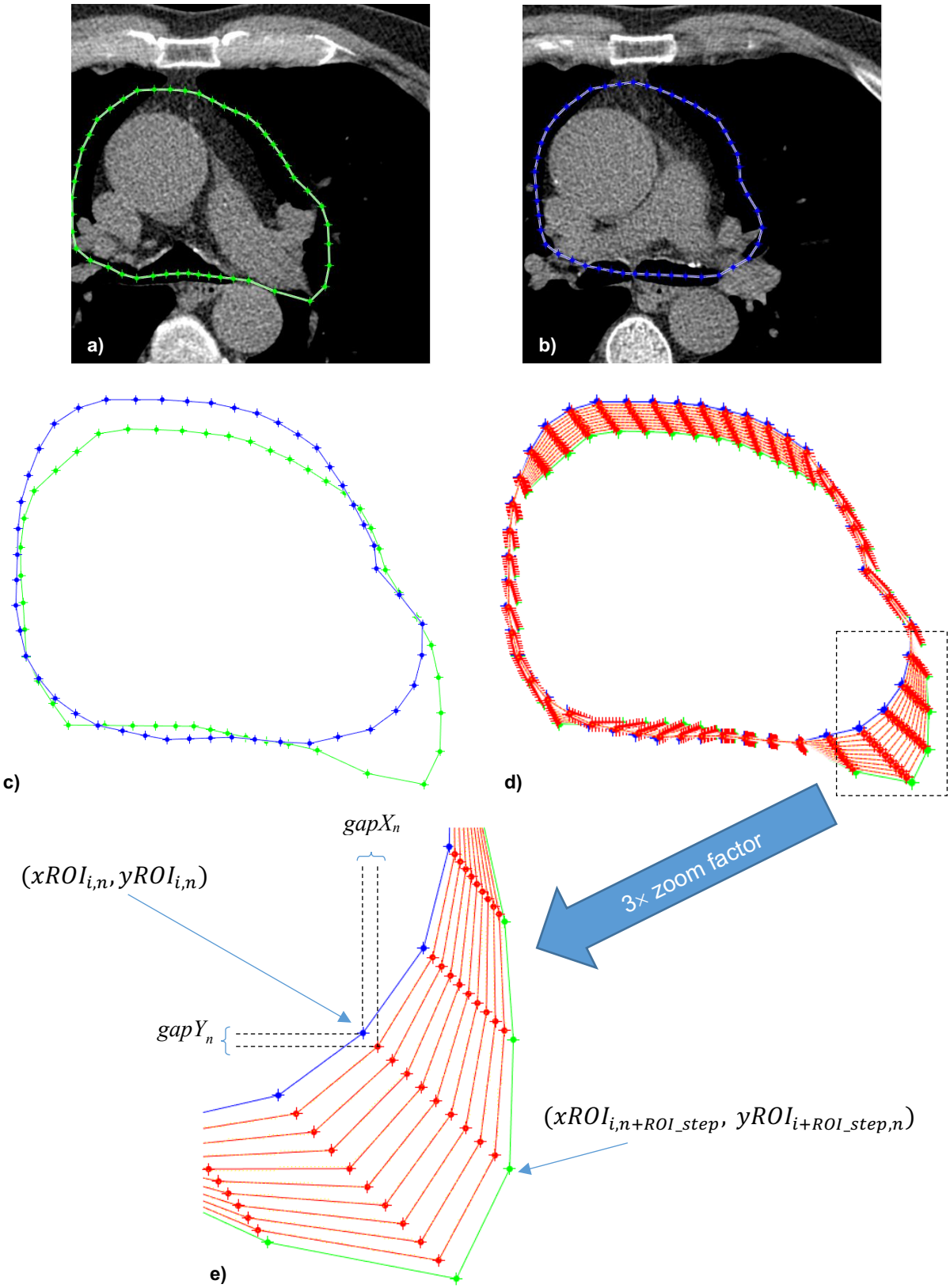

Figure 7. Interpolation steps: a) and b) the first and the last slices with the overimposed manually delineated contours; c) the ith and the $(i+ROI\_step)^{th}$ contours (with blue and green lines, respectively) manually drawn ROIs to be interpolated; d) the nine ROIs (in this case *ROI_step*=10) obtained after the interpolation process (displayed with red contour); e) zoomed area showing a detail of the obtained ROIs.

3.3. ROI Refinement

The interpolated results are reliable, and radiologists rarely need to refine one or more interpolated ROIs. In any case, to offer the possibility to perform it, an optional ROI refinement step was also implemented to increase the reliability of our system. After the refinement of a single ROI, this modification is propagated to the adjacent ROIs performing a further automatic interpolation. This additional interpolation is needed to ensure shape- and spatial-continuity among refined and unrefined ROIs. If the ROI at *current_index* position is modified, the previous and the next indices (*first_index* and *second_index,* respectively) of the previously manually placed ROIs are retrieved. By exploting these two ROIs and the refined ROI, all the ROIs included in the (*first_index*, *current_index*) and (*current_index*, *second_index*) ranges are updated (by means of a re-interpolation) according to the changes affecting the *current_index* ROI (Figure 8) and following the rationale explained in the previous section.

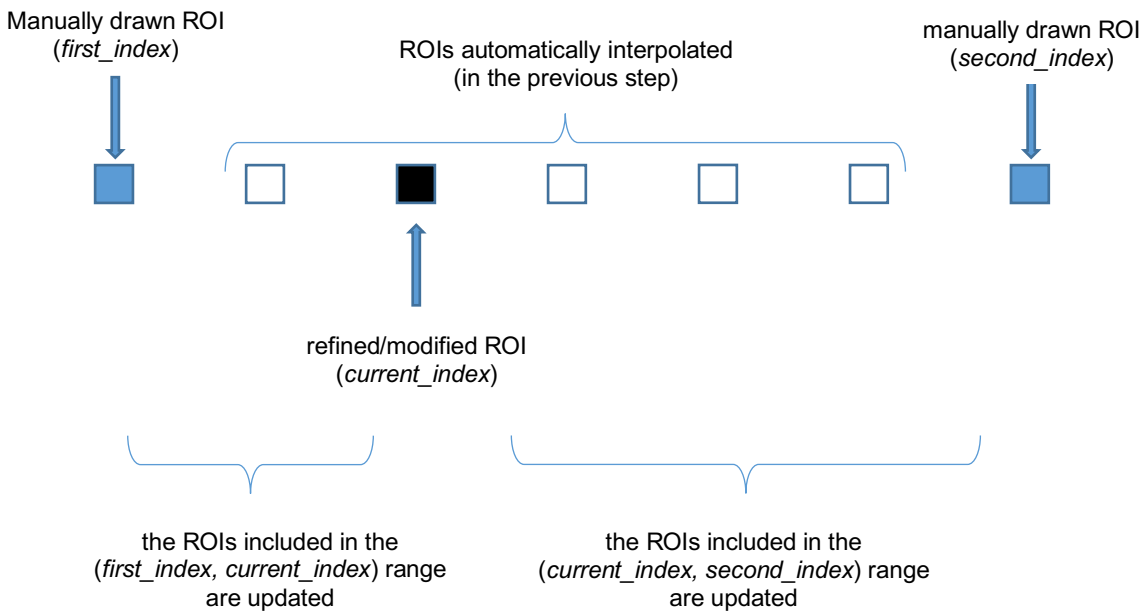

Figure 8. Interpolation strategy used to automatically update (re-interpolation) the ROIs included in the (*first_index*, *current_index*) and (*current_index*, *second_index*) ranges after performing a refinement of the ROI at *current_index* position.

3.4. Epicardial Fat Segmentation

The proposed epicardial adipose tissue segmentation approach analyzes only the area inside the ROI using an efficient double-threshold algorithm. Specifically, the voxels representing epicardial fat have HU values in the range [-190, …, -30] [43]. In general, this range is kept fixed although, in some cases, it requires to be modified by clinicians according to the different CT scanners or acquisition protocols [37]. Thus, the tool allows the radiologists to interactively modify the *min_Hounsfield* and *max_Hounsfield* parameter values, which determine the range of the HU values.

In order to enhance the achieved segmentation results, we also provide two different filtering operations that can be optionally employed by the user:

- Pre-segmentation filtering, which consists in a median filter characterized by a 5×5 convolution kernel to remove noise from CT images;
- Post-segmentation filtering, which comprises three steps: (*i*) hole filling, (*ii*) removal of small-area not representing fat voxels, (*iii*) morphological closing to smooth the ROI boundaries.

These processing steps mainly aim at dealing with artefacts due to voxel non-uniformities generated by tomographic reconstruction algorithms, such as the Filtered Back Projection (FBP) [32][44].

The output yields the overall fat volume as well as the area/volume for each analyzed image. Figure 9 shows the results of the application of the pre- and post-segmentation steps. It is noticeable that applying both these filtering steps improves segmentation results by yielding smooth boundaries and removing any hole mainly caused by pixel inhomogeneities.

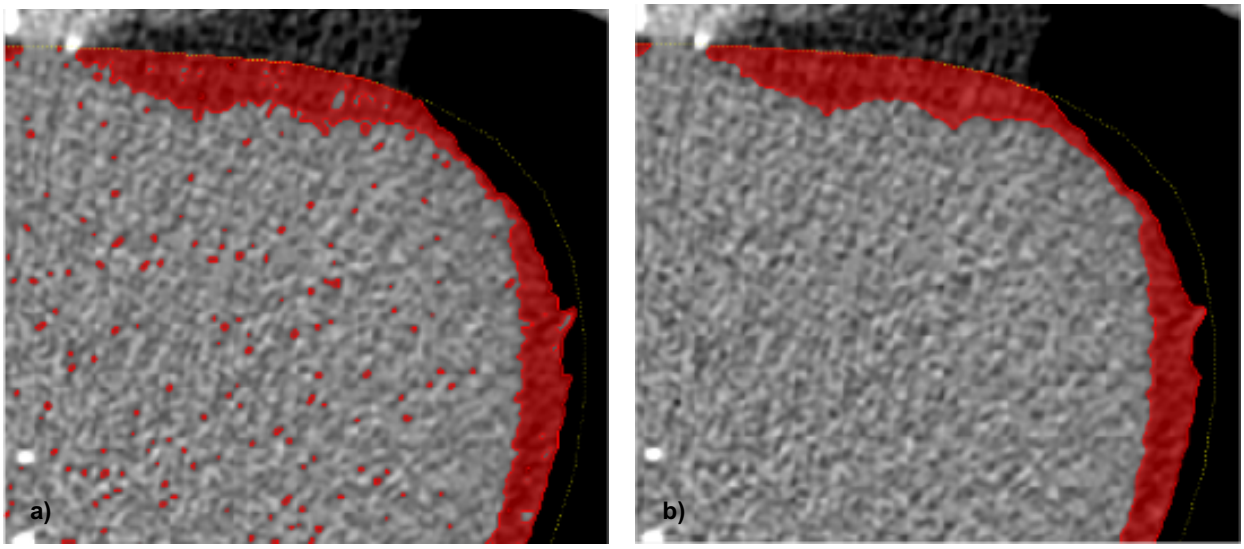

Figure 9. An example of epicardial adipose tissue segmented within the ROI. The segmented fat is contoured by solid red (dashed yellow contours represents the ROI obtained by interpolation starting from manually placed ROIs. In a) and b) segmentation result obtained without and with filtering (applying both pre-segmentation as well as post-segmentation). The images are showed with a 2× zoom factor.

3.5. Adipose Tissue Volume and Quartiles Computation

The epicardial fat segmentation is the starting-point for the following clinical analysis. The HU range of interest is by default set to [-190, …, -30] and the quartiles (indicated as Q1, Q2, Q3, and Q4) are computed accordingly. In addition, the mean HU value and the percent and the volume with respect to the whole EFV are calculated. The quartiles are denoted with different colors and over-imposed onto the current CT image.

However, the user can specify a specific quartile of interest. Figure 10 shows an instance of segmented adipose tissue with the corresponding quartiles.

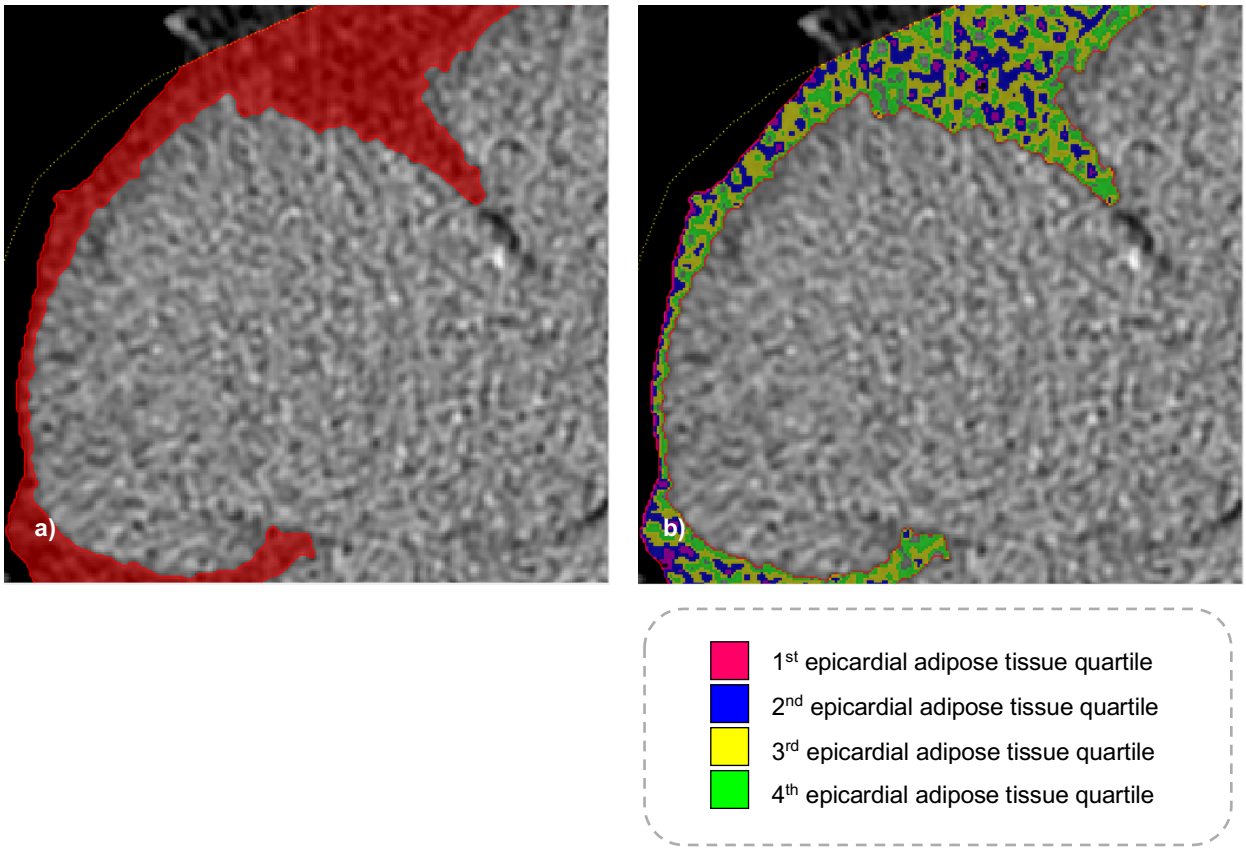

Figure 10. Epicardial adipose tissue segmentation: a) whole segmented fat; b) highlighting all the quartiles. Q1, Q2, Q3, and Q4 are denoted with magenta, blue, yellow, and green colors, respectively. The images are displayed with a 2× zoom factor.

3.6. Fat Thickness Measurement

Addressing the specific requests from cardiologists, our tool allows also for inserting a maximum of 5 measurements related to the fat thickness in some specific anatomical points, mainly in specific points of coronary arteries – e.g., right coronary artery (RCA), left descending anterior (LDA), left main (LM)) [45] – which are important to assess the clinical scenario for each examined patient. After the selection of a CT slice of interest, the clinician performs the measurements, with the possiblity to add a descriptive label on each measurement. During the quantification phase, the GUI displays several radial lines starting from the ROI centroid in order to facilitate the operation.

4. Experimental Results

In order to quantify the performance of the proposed approach, we calculated (*i*) the correlation coefficient to assess the EFV quantification performance, and (*ii*) the area-based and distance-based metrics to evaluate the

segmentation. Each semi-automatic approach requiring user intervention or feedback will involve differences, albeit minimal, due to the operator-dependence [14]. In order to reduce the bias due to this inter-observer variability, for each type of dataset, the ground-truth was manually delineated by a radiologist with at least 10 years of experience, by using a Leonardo reporting workstation (Siemens Healthcare, Erlangen, Germany) equipped with dedicated Syngo Via Cardiac (Siemens Healthcare) diagnostic software.

4.1. Dataset Characteristics

As previously introduced, the two analyzed datasets are CaSc and CorCTA. In particular, to perform experimental trials, 50 and 95 patients were retrospectively selected who underwent cardiac CT with a SOMATOM® Definition AS 128-layer scanner (Siemens Healthcare) at the University Hospital "Paolo Giaccone", University of Palermo, Palermo, Italy. Table 1 summarizes the main characteristics of the two typologies of CT scans used in our experiments. For each patient, Figures 11 and 12 depict the min/max indices (dashed lines), representing the first and the last processed slices, as well as the number of processed slices for each dataset type. The overall number of processed slices for CaSc and CorCTA datasets are 2959 and 22264, respectively. The last row of Table 1 shows the average number of ROIs set by the operator, by considering the total number of processed slices, the number of series, and the value of '*ROI_step*' parameter. These values show that the workload for the operator is minimized with respect to a fully automatic procedure, having to set (on average) about 6 (5.9) and 12 (11.7) ROIs for the CaSc and the CorCTA series, respectively.

Considering the multi-ethnicity in Sicily, which is an area characterized by a heterogeneous population due to its own genetic history [46][47], it is intuitive to expect a high variability of organ morphology. This is a critical issue to take into account, especially when dealing with atlas-based approaches, which may not represent a feasible and reliable solution due to the different portions/positions of fat in the analyzed subjects.

Table 1. Main characteristics of the two types of cardiac CT scans – CaSc and CorCTA – analyzed in this study for the EFV segmentation and quantification.

	Calcium Score (CaSc) CT scans	**Coronary Computed Tomography Angiography (CorCTA) scans**
Series number	50 (30 males and 20 females)	95 patients (68 males and 27 females)
Mean age ± standard deviation [years]	46 ± 4.17	61.6 ± 10.3
Matrix size [pixels]	512×512	512×512
Slice thickness [mm]	1.5	0.75
Total amount of processed slices	2959	22264
Processed slices per series (mean value)	~ 60	~ 235
ROI step (default)	10	20
Manually set ROIs (mean value)	5.9	11.7

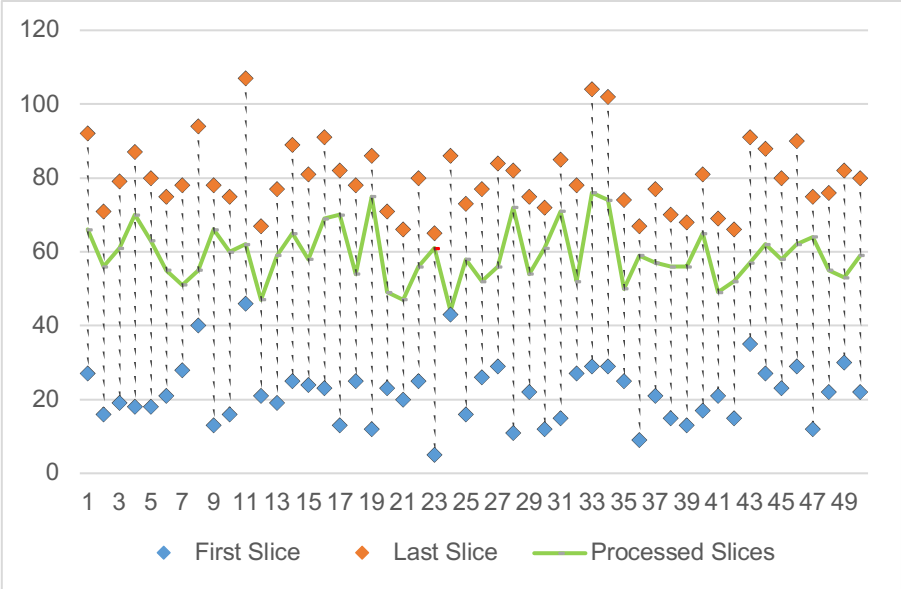

Figure 11. Range of processed slices for each patient of the CaSc dataset. This plot reports the first and the last indices of the processed slices (represented by the min/max dashed lines), as well as the number of the processed CT slices (represented by the green solid line).

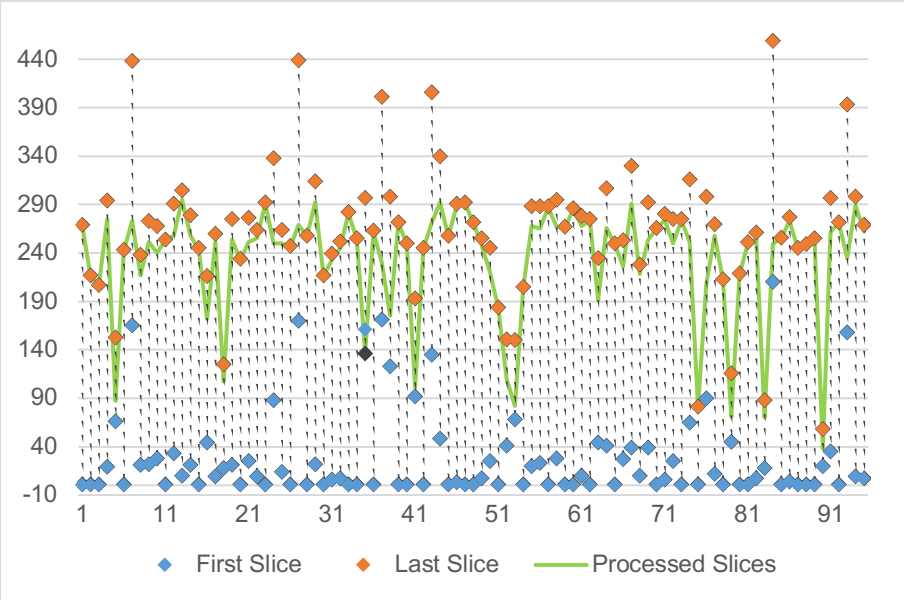

Figure 12. Range of processed slices for each patient of the CorCTA dataset. This plot reports the first and the last indices of processed slices (represented by the min/max dashed lines), and the number of the processed CT slices (represented by the green solid line).

Before quantitatively evaluating the achieved experimental results, it was worth to quantify the 'noise level' of the images, by calculating the Signal-to-Noise-Ratio (SNR) on all the processed CT (CaSC and CorCTA) images, in order to highlight the variability of the image signal and, consequently, the robustness and reliability of the proposed approach. In particular, the used SNR is defined in Eq. (5) [48][49]. The results, represented by the boxplots in Figure 13, reveal the variability across the CT series included in the analyzed datasets.

$$SNR = \frac{\mu_{ROI}}{\sigma_{ROI}}. \quad (5)$$

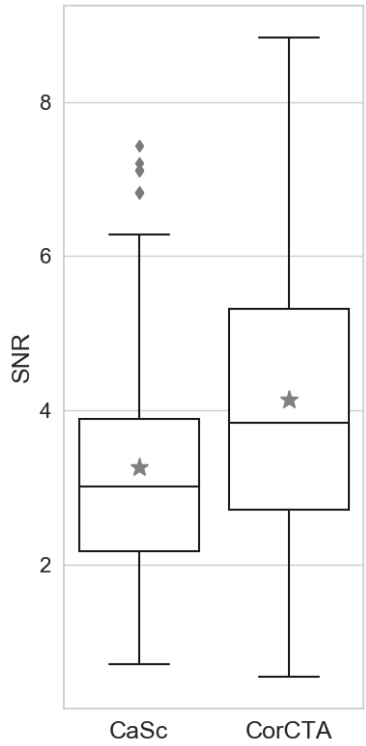

Figure 13. SNR values obtained on the two types of datasets (CaSc and CorCTA) used for EFV quantification. The black line and the gray star denote the median and the mean values, respectively.

4.2. Computation Times and Memory Consumption

This section provides some details concerning the average processing times and memory consumption for each of the main steps of the whole processing pipeline. Table 2 shows the results averaged over 10 different CT series for each of the two dataset types, without taking into account the optional steps (i.e., ROI Refinement, Fat Thickness Measurement). The computational tool exploiting the proposed approach was deployed on a computational platform with an Intel i7@2.4 GHz CPU, 8 GB RAM and Microsoft Windows 10 operating system.

As reported in Table 2, the analyzed CaSc and CorCTA datasets have approximately 60 and 235 slices, respectively, and the parameter *ROI_step* was set to the default value (i.e., the user has to manually draw about 7 and 13 ROIs for the CaSc and CorCTA, respectively). The overall mean time required by the proposed semi-automatic approach and by the fully manual procedure is ~3.5 minutes and ~14.5 minutes, respectively, for the CaSc cases. Thus, thanks to our smart and reliable interpolation strategy that avoids the manual delineation of all the ROIs, the achieved speed-up is ~4.3×. Similarly, the overall mean time required by the proposed semi-automatic approach and by the fully manual procedure is ~7.4 minutes and ~55.3 minutes, respectively, for the CorCTA cases. Thus, the achieved speed-up is ~7.5×. As a matter of fact, the 'ROI Selection' and 'ROI

Interpolation' steps are the most time-consuming. Moreover, by relying on the MatLab '`workspace`' built-in function, the memory required by the EFV computation and quantification was assessed. Table 3 shows that the increase of the memory consumption during the different processing phases is related to the variables allocated to store the output of each step. In particular, as expected, the 'ROI Interpolation' requires the highest amount of memory. As a matter of fact, after the interpolation phase, many variables (needed only for the ROI interpolation) are deallocated and the total memory consumption decreases. It must be considered that the average size of the processed CT series is 35 MB and 120 MB for CaSC and CorCTA, respectively.

Table 2. Comparison of the average processing times required by the proposed approach and the corresponding fully manual approach without the interpolation phase, where a ROI is manually traced on every slice.

Processing steps	**CaSc dataset**		**CorCTA dataset**	
Processing steps	**Fully manual approach average processing time [s]**	**Proposed approach average processing time [s]**	**Fully manual approach average processing time [s]**	**Proposed approach average processing time [s]**
CT Series Loading	14.04		26.20	
ROI Selection	852.63	112.54	3274.91	149.45
ROI Interpolation	0	70.96	0	253.18
Epicardial Adipose Tissue Segmentation	3.66		10.28	
Fat Volume and Quartiles Computation	1.95		5.37	
Total Processing Time	**872.28**	**203.15**	**3316.76**	**444.48**

Table 3. Average memory consumption for each of the main processing phases for the CaSc and CorCTA dataset analysis.

Processing steps	**CaSC Dateset Average Memory Consumption [MB]**	**CorCTA Dateset Average Memory Consumption [MB]**
Opened EVF Segmentation Tool	222	243
CT Series Loading	514	1063
ROI Selection	738	1370
ROI Interpolation	1043	2451
Epicardial Adipose Tissue Segmentation	866	1651
Fat Volume and Quartiles Computation	871	1638

4.3. Segmentation Evaluation

In order to evaluate the accuracy of the EFV segmentation, area-based and distance-based metrics were used [50]. Moreover, to correlate the overall EFV against the ground-truth the scatter diagrams were plotted as well as the Pearson and Spearman correlation coefficients were calculated.

4.3.1. Spatial -based and Distance-based Metrics

Area-based metrics compare the regions segmented (R_{Auto}) by the proposed approach against the ground-truth (R_{GT}) manually segmented by a physician/radiologist. In order to obtain the ground-truth, required to define a reference to compare the segmentation result obtained by the proposed semi-automatic approach, the cardio-CT examinations were evaluated by a radiologist with a training of at least 10 years.

Let I be the image to be analyzed, the region containing "true positives" is defined as:

$$R_{TP} = R_{Auto} \cap R_{GT}.$$

The *DSC*, the most used statistics in validating medical volume segmentations, can be defined as:

$$DSC = \frac{2|R_{TP}|}{|R_{Auto}| + |R_{GT}|}. \tag{6}$$

In addition to area-based metrics, which take into account the spatial position of the boundary voxels, distance-based metrics should be utilized when the boundary delineation is critical. Accordingly, the distance between the boundaries computed by the proposed segmentation method and the ones delineated by the expert is calculated. These boundaries are formally defined by the vertices $A = \{\mathbf{a}_i : i = 1,2,\ldots,K\}$ and $T = \{\mathbf{t}_j : j = 1,2,\ldots,N\}$, respectively. The distance between an element of the contour relative to the automatically calculated ROI $\mathbf{a}_i \in A$ and the point set T is defined in Eq. (7):

$$d(\mathbf{a}_i, T) = \min_{j \in \{1,\ldots,N\}} \left\| \mathbf{a}_i - \mathbf{t}_j \right\|. \tag{7}$$

We used the Mean Absolute Distance (*MAD*) to quantify the average error in the segmentation process, defined in Eq. (8), where: $d(\mathbf{t},\mathbf{a}) = \|\mathbf{t} - \mathbf{a}\| = \sqrt{\sum_{k=1}^{n} (t_k - a_k)^2}$ is a norm.

$$MAD = \frac{1}{K} \sum_{i=1}^{K} d(\mathbf{a}_i, T) \tag{8}$$

Table 4 depicts the mean and standard deviation values of area-based and distance-based metrics obtained in the experimental tests. The distance-based metrics are consistent with area-based metrics, by demonstrating

that good performance was obtained also in terms of difference between semi-automated and manual boundaries. Overall, the achieved segmentation performance shows the accuracy and reliability of the proposed semi-automatic approach.

Table 4. Spatial area-based and distance-based metrics achieved by the proposed semi-automatic approach.

Segmentation Evaluation Metrics	CaSc Dataset	CorCTA Dataset
DSC	93.74%	92.48%
MAD	2.18	2.87

4.3.2. EFV Quantification Evaluation

To evaluate the quantified EFV, we calculated the Pearson and Spearman correlation coefficients between the overall ground-truth volume (V_{GT}) and the segmented volume (V_{Auto}) measurements. Figures 14 and 15 show the scatter diagrams concerning V_{Auto} versus V_{GT} on the CaSc and CorCTA datasets, respectively.

The achieved results show a high level of correlation between our semi-automatic method and the ground-truth obtained by means of manual delineation. Details about the Pearson and Spearman correlation coefficients are depicted in Table 5.

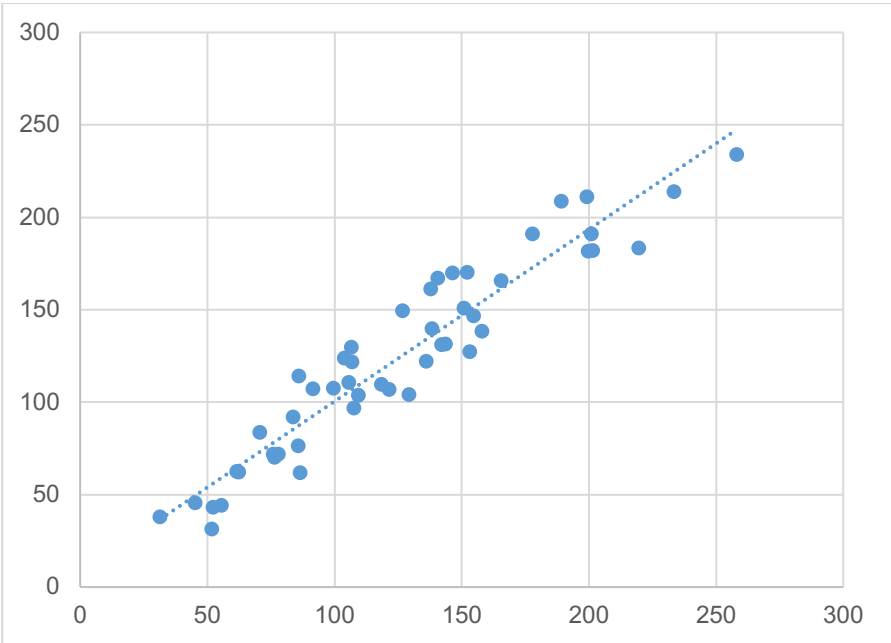

Figure 14. Scatter diagram obtained on the CaSc CT dataset showing the correlation between the overall epicardial adipose tissue volume (in cm^3) calculated using the proposed semi-automatic approach (abscissa axis) against the ground-truth volume (ordinate axis). The values were obtained on 50 patients (30 males and 20 females) underwent cardiac-CT examination. The obtained Pearson and Spearman correlation coefficients are 0.9591 and 0.9490, respectively. The dashed line represents the equality line.

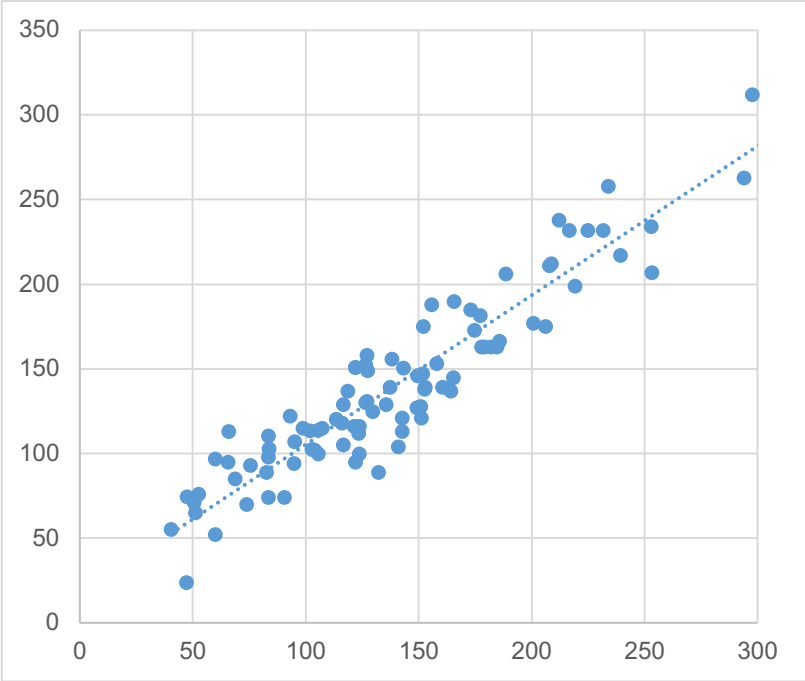

Figure 15. Scatter diagram obtained on the CorCTA dataset showing the correlation between the overall epicardial adipose tissue volume (in cm^3) calculated with the proposed semi-automatic approach (abscissa axis) against the ground-truth volume (ordinate axis). The values were obtained on 95 patients (68 males and 27 females) underwent cardiac-CT examination. The obtained Pearson and Spearman correlation coefficients are 0.9513 and 0.9319, respectively. The dashed line represents the equality line.

Table 5. Pearson and Spearman correlation coefficients achieved by the proposed semi-automatic approach.

EFV Correlations	CaSc Dataset	CorCTA Dataset
Pearson coefficient (p<0.0001)	0.9591	0.9513
Spearman's rho (p<0.0001)	0.9490	0.9319

5. Discussions and Comparisons

The quantification of the cardiac adipose tissue represents an interesting and active research topic, mainly for the consequences related to people health. In fact, recent findings have shown a growing interest in the study of adipose tissue, by indicating a strong correlation between the risk of future heart diseases and the volume of adipose tissue inside the pericardium [6][7]. For completeness, Table 6 summarizes the characteristics of literature approaches dealing with EFV segmentation and quantification.

Our goal is to show the trend in the literature even in different clinical scenarios and experimental settings. For this reason, we summarized the results obtained by the works addressing the same issue. In fact, Table 6 shows the data and results from the original publications as they are, aiming at providing an overview of the state-of-the-art methods for EFV segmentation and quantification. More interestingly, a taxonomy based on the degree of user interaction (i.e., automatic or semi-automatic) and the underlying computational framework (i.e., model-based, supervised/unsupervised model, basic image analysis) is provided.

Moreover, to the best of our knowledge, public CT imaging datasets for epicardial fat segmentation to be used as benchmark are not currently available for performing a comparative analysis on the same training and testing data.

Manual reporting procedures are more time-consuming than computer-assisted approached and are affected by an intrinsic inter-operator dependency that could lead to inconsistencies in the obtained results. For this reason, the best choice should be the development of computer-assisted methods helping clinicians in the quantification tasks, so reducing the inter-operator dependency. In [14] an interesting work is proposed where a semi-automatic method is used to evaluate the effect of scanning protocols and the observer variability in EFV quantification. For this reason, the correlations between the EFVs, obtained by two different operators on two dataset types, are reported and discussed. It must be pointed out that the ROIs are placed manually on MPRs of the original images. Considering the obtained findings, where a strong correlation between results was shown, the authors stated that on both datasets' types the approach can be used for EFV measurement in the clinical routine, thanks to its low intra- and inter-observer variability.

Table 6. Main characteristics of the analyzed literature EFV segmentation and quantification methodologies. A taxonomy based on the degree of user interaction and the underlying computational model is provided.

Reference	Methodology	Segmentation approach	Dataset type	Training or development samples	Test samples	Correlation coefficient	DSC/MAD values
D'Errico et al. [15]	semi-automatic basic image analysis	manual ROIs + thresholding	coronary CTA non-contrast cardiac CT	0	30	0.99	N.A.
Ding et al. [16]	automatic atlas-based	atlas-based + graph-based	MR angiography	4	6	0.89	DSC=82 ± 6
Norlén et al. [30]	automatic supervised model	multi-atlas + random forest	CT angiography	20	30	0.99	DSC=91± 4
Rodrigues et al. [31]	automatic supervised model	atlas-based + features-based segmentation	CT	20 (878 images)	N.A.[1]	N.A.	DSC=97.6
Shahzad et al. [32]	automatic basic image analysis	multi-atlas + thresholding	CT	8	98	0.91	DSC=89.1 DSC=89.2
Zlokolica et al. [35]	semi-automatic unsupervised model	FCM clustering + geometric modeling	CT	0	10	N.A.	DSC=69
Coppini et al. [37]	semi-automatic basic image analysis	thresholding and level set segmentation	calcium score CT	0	10	N.A.	N.A.
Proposed approach	**semi-automatic basic image analysis**	**thresholding segmentation**	**calcium score CT**	**0**	**50 (2959 images)**	**Pearson=0.9591 Spearman=0.9490**	**DSC=93.74 MAD=2.18**
			coronary CTA	**0**	**95 (22264 images)**	**Pearson=0.9513 Spearman=0.9319**	**DSC=92.48 MAD=2.87**

[1] It is not clear the number of patient used in the testing phase. The authors literally report only that '2.5 gigabytes originated from the patients of the ground truth'

The literature proposes different approaches, both automatic [16][30][31][32][33] and semi-automatic [15][35][37], for the EFV quantification. All automatic approaches are based either on atlases, exploited to identify the ROI where the epicardial fat tissue must be detected, or on Deep Learning methods. Even though fully automatic procedures can considerably reduce the processing time, they could introduce significant errors under unexpected clinical scenarios, since they do not allow for any human interactive feedback.

Generally, the use of atlases for ROI detection starts from the assumption that there is a common model in which all the analyzed cases can be mapped. As soon as the analyzed patient has morphological characteristics that are different from the atlas model, then the quantification of the fat volume may present deviations with respect to the ground-truth [20][21]. As a result, inaccurate segmentation results could occur.

In order to improve the performance and avoid future unpredicted events, such as deformations in the retrosternal area, the authors of [31] applied a confirmation method relying on distance-based heuristics and the orientation of neighboring pixels. Furthermore, it is worth to note that two different techniques were used for the quantification of the system accuracy on a single patient: a 10-fold cross-validation and a 66% split of the patient data. Ground-truth and training were performed on 20 patients (878 images). However, the number of patients/images used for the testing phase is unknown.

Deep Learning methods are gaining ground in cardiovascular imaging [33]. With particular reference to the image segmentation and quantification tasks, the Multi-Modality Whole Heart Segmentation (MM-WHS) challenge has been recently organized by the International Conference on Medical Image Computing and Computer-Assisted Intervention (MICCAI) 2017 [34]. This competition involved the whole heart segmentation on 60 CT and 60 MRI scans, aiming at a fair comparison among different computational methods as well as contributing to collect a benchmark for both modalities.

On the one hand, the methods based on Deep Learning exhibited great potential, but several of them reported poor performance in the blinded evaluation on unseen test data (probably due to overfitting in the training/development phase): indeed, the performance is highly dependent on network architectures and training strategies. On the other hand, the conventional algorithms, mainly based on multi-atlas segmentation, achieved robust and stable results (also in the case of highly variable scenarios), even though the accuracy and computational complexity might represent limitations.

Nevertheless, the epicardial fat is not considered among the segmented structures in the MM-WHS challenge and no method based on Deep Learning has been proposed so far.

A limitation of semi-automatic approaches is the need for the operator intervention that could typically involve higher processing times with respect to computationally-efficient fully automated approaches. Generally, in the first steps of the semi-automatic pipelines, some ROIs or control points must be selected in order to provide the necessary information to the algorithms exploited by the subsequent automated processing phase for obtaining the EFV.

Moreover, an underestimated, yet very important, aspect is that the training and test sets are used as a statistical basis to evaluate the approach. An inadequate database could lead to misleading results. In [16] and [30] the ratio between training/development and test samples is too high: 4/6 and 20/30 respectively (i.e., 2/3 in both

cases). Very similar situations are observed in [35] and [37], wherein only 10 samples are used in the experimental tests. In order to define a statistically significant basis to validate the computational method, the tests should be carried out on more cases. Our approach has been tested on 145 samples, by processing overall over 25,000 CT images. Considering the large amont of the processed slices, even compared to similar works of literature, the results obtained, both in terms of quality of the segmentation and correlation with the ground-truth, are excellent and reliable.

The proposed semi-automatic approach requires the intervention of the operator in the initial step to set the reference ROIs. The interactive tool implemented allows the operator to effectively interact in this phase and correct, when necessary, the ROIs aiming at obtaining a greater precision in quantification.

Moreover, as shown in Table 1, unlike a fully manual procedure, the proposed approach allows us to reduce the ROIs to be delineated manually by a '*ROI_Step*' factor. Considering that each CT series has about 60 and 235 images (i.e., for the CaSC and CorCTA series, respectively), the workload for the operator is highly reduced, having to set (on average) only 6 (5.9) ROIs for the CaSc series and 12 (11.7) ROIs for the CorCTA series.

Naturally, the operator feedback required to manually set and adjust the reference ROIs is an aspect to take into account for any semi-automatic strategy, leading to longer processing times compared to a fully automatic strategy. However, our approach allows us to assist and automate a procedure still manual in the clinical routine. In order to provide an estimate of the average time needed to process a CT series, an evaluation was performed by considering 10 CaSc series and 10 CotCTA series. The obtained average processing times are about 3.5 and 7.5 minutes for CaSC and CorCTA, respectively, when any ROI refinement is required.

The proposed method appropriately combines literature methods and new approaches (such as in the interpolation step) in a smart and efficient way, in order to tackle the problem of epicardial fat segmentation. The combination of computational techniques and the application scenario make our approach effective and efficiently to solve this challenging problem. This evidence is supported by the achieved experimental results, also considering that our approach has neither initial training nor setup.

The clinical feasibility has always been always taken into account in the design choices, so leading to a solution based on a semi-automatic strategy that allows for a safe end-user control of the automated result. Our computational solution, which does not require any training/setup phase, considerably facilitates the direct translation and deployment of the approach into the clinical practice [27]. This important aspect is endorsed by the compelling issues related to the explainability of Artificial Intelligence methods in medicine that must be taken into account for the adoption and the clinical feasibility of a novel Clinical Decision Support System (CDSS) [51]. Moreover, our software solution used a user-centred Graphical User Interface (GUI) design, allowing us to optimize the GUIs for a safe interaction by the physician (user experience) as well as for an effective integration into the existing clinical workflow [52].

6. Conclusions and Future Work

The growing interest in the study of epicardial adipose tissue is mainly motivated by the increase in the incidence of related cardiovascular diseases. In fact, literature works have shown a direct association between epicardial fat and risk of major cardio- and cerebro-vascular diseases [53]. In addition, the thickness of epicardial fat determines also a higher risk of heart disease [54]. Recent studies exhibited a correlation between the thickness of epicardial adipose tissue and the incidence of non-coronary artery cardiac disease such as atrial fibrillation, probably linked to the increased production of activin A by epicardial adipose tissue, which has a pro-fibrotic effect on atrial myocardium [55][56].

These are just the main motivations making EFV segmentation and quantification a hot research topic. As a matter of fact, in the future, the EFV quantification may become a therapeutic target of pharmacological therapies that can act with a positive synergism on the different factors responsible for cardiovascular diseases [6][7].

Considering these premises, the objective of our study was to develop an approach for supporting the clinicians in screening programs of patients' categories with cardiovascular risk factors. The EFV quantification could help the cardiologist to gain an in-depth knowledge into the analyzed clinical scenario, representing a necessary condition to realize a personalized therapy based on patient-specific characteristics.

Accordingly, we implemented a clinically feasible tool, based on the proposed semi-automatic method, able to assist clinicians in the EFV quantification routine. Our approach automates and assists the fat detection and quantification task, allowing the physician to keep control of every processing step; these conditions are necessary for clinically feasible and interpretable solutions. Moreover, our design choices overcome some typical problems of fully automatic approaches: since any *a priori* or learned knowledge for the setup phase of the system (e.g., model construction for atlas-based approaches or training in supervised Machine Learning approaches) is needed, the approach can be immediately used in the clinical practice.

The achieved experimental results, in terms of area-based and distance-based metrics as well as the correlation between quantified EFV and ground-truth, show the accuracy and reliability of the proposed semi-automatic approach. Moreover, differently from the existing methods, our approach automatically computes both the whole EFV and its quartiles. EFV quantification and fat quartiles analysis are clinically useful functionalities for the near future: these novel tools will allow clinicians to conduct in-depth analyses, as well as to establish meaningful associations between fat density and volume quartiles according to the clinical scenario.

The current design choices require the user input for the selection of the initial target ROIs that, by means of a smart interpolation process, are suitably extended over all the slices to be examined. In the near future, the authors aim at further improving this computer-assisted segmentation approach, developing an automatic strategy for the detection of the bounding region containing the heart [57]. The automatic definition of this volume would eliminate any dependency of intervention by the operator. For instance, a CNN-based approach could be exploited to this purpose. However, the system should be trained by providing annotated input datasets along with the corresponding gold standard segmentation. Considering the inherent 'morphological variability' that may be found in the anatomical district of interest, a suitable training set of representative cases, both in terms of number and diversity, should be provided to cover (mostly) every situation that the

neural network could encounter, so allowing for good generalization abilities. It is important to bear in mind that, even in the case of a fully automatic system aiming at the clinical feasibility and applicability, the human feedback is always necessary to validate the result of the computer-assisted system. In this way, the clinicians will be provided with an even more advanced tool, capable of further reducing the user-dependence as well as the required workload.

Lastly, the high-throughput extraction of additional features on the CT density (i.e., HU) by means of radiomics approaches might definitely be of clinical interest for performing advanced Machine Learning analyses aiming at precision medicine [58].

Conflict of Interest Disclosure

All authors in this paper have no potential conflict of interest.

References

[1] G.A. Rosito, J.M. Massaro, U. Hoffmann, F.L. Ruberg, A.A. Mahabadi, R.S. Vasan, C.J. O'Donnell, C.S. Fox, Pericardial fat, visceral abdominal fat, cardiovascular disease risk factors, and vascular calcification in a community-based sample: the Framingham Heart Study, Circulation 117 (5) (2008) 605–613. doi: 10.1161/CIRCULATIONAHA.107.743062

[2] M.L. Kortelainen, Myocardial infarction and coronary pathology in severely obese people examined at autopsy, Int. J. Obes. Relat. Metab. Disord. 26 (1) (2002) 73–79. doi: 10.1038/sj.ijo.0801852

[3] G. Iacobellis, D. Pistilli, M. Gucciardo, F. Leonetti, F. Miraldi, G. Brancaccio, P. Gallo, C.R.T. di Gioia. Adiponectin expression in human epicardial adipose tissue in vivo is lower in patients with coronary artery disease, Cytokine 29 (6) (2005) 251–255. doi: 10.1016/j.cyto.2004.11.002

[4] J. Ding, S.B. Kritchevsky, T.B. Harris, G.L. Burke, R.C. Detrano, M. Szklo, J.J. Carr, The association of pericardial fat with calcified coronary plaque, Obesity 16 (8) (2008) 1914–1919. doi: 10.1038/oby.2008.278

[5] D. Dey, N.D. Wong, B. Tamarappoo, R. Nakazato, H. Gransar, V.Y. Cheng, A. Ramesh, I. Kakadiaris, G. Germano, P.J. Slomka, D.S. Berman, Computer-aided non-contrast CT-based quantification of pericardial and thoracic fat and their associations with coronary calcium and metabolic syndrome, Atherosclerosis 209 (1) (2010) 136–141. doi: 10.1016/j.atherosclerosis.2009.08.032

[6] F. Mookadam, R. Goel, M.S. Alharthi, P. Jiamsripong, S. Cha, Epicardial fat and its association with cardiovascular risk: a cross-sectional observational study, Heart Views 11 (3) (2010) 103–8. doi: 10.4103/1995-705X.76801

[7] R. Sicari, A.M. Sironi, R. Petz, F. Frassi, V. Chubuchny, D.D. Marchi, V. Positano, M. Lombardi, E. Picano, A. Gastaldelli, Pericardial rather than epicardial fat is a cardiometabolic risk marker: an MRI vs echo study. J. Am. Soc. Echocardiogr. 24 (10) (2011) 1156–1562. doi: 10.1016/j.echo.2011.06.013

[8] L.L. Geyer, U.J. Schoepf, F.G. Meinel, J.W. Nance Jr, G. Bastarrika, J.A. Leipsic, N.S. Paul, M. Rengo, A. Laghi, C.N. De Cecco. State of the art: iterative CT reconstruction techniques, Radiology 276 (2) (2015) 339–357. doi: 10.1148/radiol.2015132766

[9] F. Boas, D. Fleischmann, CT artifacts: Causes and reduction techniques, Imaging Med. 4 (2) (2012) 229–240. doi: 10.2217/iim.12.13

[10] K. Ueno, T. Anzai, M. Jinzaki, M. Yamada, Y. Jo, Y. Maekawa, A. Kawamura, T. Yoshikawa, Y. Tanami, K. Sato, S. Kuribayashi, S. Ogawa, Increased epicardial fat volume quantified by 64-multidetector computed tomography is associated with coronary atherosclerosis and totally occlusive lesions, Circ. J. 73 (10) (2009) 1927–1933.

[11] S. Sarin, C. Wenger, A. Marwaha, A. Qureshi, B.D. Go, C.A. Woomert, K. Clark, L.A. Nassef, J. Shirani, Clinical significance of epicardial fat measured using cardiac multislice computed tomography, Am. J. Cardiol. 102 (6) (2008) 767–771. doi: 10.1016/j.amjcard.2008.04.05

[12] É.O. Rodrigues, V.H.A. Pinheiro, P. Liatsis, A. Conci, Machine learning in the prediction of cardiac epicardial and mediastinal fat volumes, Comput. Biol. Med. 89 (2017) 520–529. doi: 10.1016/j.compbiomed.2017.02.010

[13] L. La Grutta, P. Toia, A. Farruggia, D. Albano, E. Grassedonio, A. Palmeri, E. Maffei, M. Galia, S. Vitabile, F. Cademartiri, M. Midiri, Quantification of epicardial adipose tissue in coronary calcium score and CT coronaryangiography image data sets: comparison of attenuation values, thickness and volumes. Br. J. Radiol. 89 (1062) (2016) 20150773. doi: 10.1259/bjr.20150773

[14] G. Milanese, M. Silva, L. Bruno, M. Goldoni, G. Benedetti, E. Rossi, C. Ferrari, L. La Grutta, E. Maffei, P. Toia, E. Forte, R.C. Bonadonna, N. Sverzellati, F. Cademartiri, Quantification of epicardial fat with cardiac CT angiography and association with cardiovascular risk factors in symptomatic patients: from the ALTER-BIO (Alternative Cardiovascular Bio-Imaging markers) registry, Diagn. Interv. Radiol. 25 (1) (2019) 35–41. doi: 10.5152/dir.2018.18037

[15] L. D'Errico, F. Salituri, M. Ciardetti, R. Favilla, A. Mazzarisi, G. Coppini, C. Bartolozzi, P. Marraccini, Quantitative analysis of epicardial fat volume: effects of scanning protocol and reproducibility of measurements in non-contrast cardiac CT vs. coronary CT angiography, Quant. Imaging Med. Surg. 7 (3) (2017) 326–335. doi: 10.21037/qims.2017.06.08

[16] X. Ding X, J. Pang, Z. Ren, M. Diaz-Zamudio, C. Jiang, Z. Fan, D.S. Berman, D. Li, D. Terzopoulos, P.J. Slomka, D. Dey, Automated pericardial fat quantification from coronary magnetic resonance angiography: feasibility study, J. Med. Imaging 3 (1) (2016) 014002. doi: 10.1117/1.JMI.3.1.014002

[17] A. Cristobal-Huerta, A. Torrado-Carvajal, N. Malpica, M. Luaces, J.A. Hernandez-Tamames, Automated quantification of epicardial adipose tissue in cardiac magnetic resonance imaging. Proc. 37th Annual International Conference of the IEEE Engineering in Medicine and Biology Society (EMBC), 2015, pp. 7308–7311. doi: 10.1109/EMBC.2015.7320079

[18] T. Teme T, B. Sayegh, M. Syed, D. Wilber, L. Bakhos, M. Rabbat, Quantification of epicardial fat volume using cardiovascular magnetic resonance imaging, J. Cardiovasc. Magn. Reson. 16 (Suppl 1) (2014) O112. doi:10.1186/1532-429X-16-S1-O112

[19] T. Rohlfing, R. Brandt, R. Menzel, D.B. Russakoff, C.R. Maurer, Quo vadis, atlas-based segmentation?, In Handbook of Biomedical Image Analysis, pp.435–486. Topics in Biomedical Engineering International Book Series. Springer, Boston, MA, USA. doi: 10.1007/0-306-48608-3_11

[20] M. Antonelli, M.J. Cardoso, E.W. Johnston, M.B. Appayya, B. Presles, M. Modat, S. Punwani, S. Ourselin, GAS: A genetic atlas selection strategy in multi-atlas segmentation framework, Med. Image Anal. 52 (2019) 97–108. doi: 10.1016/j.media.2018.11.007

[21] P. Liang, L. Shi, N. Chen, Y. Luo, X. Wang, K. Liu, V.C.T. Mok, W.C.W. Chu, D. Wang, K. Li, Construction of brain atlases based on a multi-center MRI dataset of 2020 Chinese adults, Sci. Rep. 5 (2015) 18216. doi: 10.1038/srep18216

[22] Z. Xiong, V.V. Fedorov, X. Fu, E. Cheng, R. Macleod, J. Zhao, Fully automatic left atrium segmentation from late gadolinium enhanced magnetic resonance imaging using a dual fully convolutional neural network, IEEE Trans. Med. Imaging 38 (2) (2019) 515-524. doi: 10.1109/TMI.2018.2866845

[23] H. Li, A. Li, M. Wang, A novel end-to-end brain tumor segmentation method using improved fully convolutional networks, Comput. Biol. Med. 108 (2019) 150–160. doi: 10.1016/j.compbiomed.2019.03.014.380

[24] Y. Tang, C. Hojatkashani, I.D. Dinov, B. Sun, L. Fan, X. Lin, H. Qi, X. Hua, S. Liu, A.W. Toga, The construction of a Chinese MRI brain atlas: a morphometric comparison study between Chinese and Caucasian cohorts, NeuroImage 51 (2010) 33–41. doi: 10.1016/j.neuroimage.2010.01.111

[25] J. Bai, M.F. Abdul-Rahman, A. Rifkin-Graboi, Y.S. Chong, K. Kwek, S.M. Saw, K.M. Godfrey, P.D. Gluckman, M.V. Fortier, M.J. Meaney, A. Qiu, Population differences in brain morphology and microstructure among Chinese, Malay, and Indian neonates, PLoS One (2012) 7 e47816. doi: 10.1371/journal.pone.0047816

[26] R. Takahashi, K. Ishii, T. Kakigi, K. Yokoyama, Gender and age differences in normal adult human brain: voxel-based morphometric study, Hum. Brain Mapp. 32 (7) (2011) 1050–1058. doi: 10.1002/hbm.21088

[27] B. Allen Jr, S.E. Seltzer, C.P. Langlotz, K.P. Dreyer, R.M. Summers, N. Petrick, et al., A road map for translational research on artificial intelligence in medical imaging: from the 2018 National Institutes Research of Health/RSNA/ACR/The Academy Workshop, J. Am. Coll. Radiol. (2019) 1–11 (In press). doi: 10.1016/j.jacr.2019.04.014

[28] F.B. Assunção, D.C.L. de Oliveira, V.F. Souza, M.S. Nacif, Cardiac magnetic resonance imaging and computed tomography in ischemic cardiomyopathy: an update, Radiol. Bras. 49 (1) (2016) 26–34. doi: 10.1590/0100-3984.2014.0055

[29] R. Fischbach, S. Miller, M. Beer, J. Lotz, D. Kivelitz, Recommendations of the Heart Diagnosis Working Group of the German Roentgen Society for use of computerized tomography and magnetic resonance tomography in heart diagnosis. 1 – Computerized tomography, Fortschr. Röntgenstr. 181 (7) (2009) 700-706. doi: 10.1055/s-0028-1109533

[30] A. Norlén, J. Alvén, D. Molnar, O. Enqvist, R.R. Norrlund, J. Brandberg, G. Bergström, F. Kahl, Automatic pericardium segmentation and quantification of epicardial fat from computed tomography angiography, J. Med. Imaging 3 (3) (2016) 034003. doi: 10.1117/1.JMI.3.3.034003

[31] É.O. Rodrigues, F.F. Morais, N.A. Morais, L.S. Conci, L.V. Neto, A. Conci, A novel approach for the automated segmentation and volume quantification of cardiac fats on computed tomography, Comput. Methods Programs Biomed. 123 (2016) 109–28. doi: 10.1016/j.cmpb.2015.09.017

[32] R. Shahzad, D. Bos, C. Metz, A. Rossi, H. Kirisli, A. van der Lugt, S. Klein, J. Witteman, P. de Feyter, W. Niessen, L. van Vliet, T. van Walsum, Automatic quantification of epicardial fat volume on non-enhanced cardiac CT scans using a multi-atlas segmentation approach, Med. Phys. 40 (9) (2013) 091910. doi: 10.1118/1.4817577

[33] S.J. Al'Aref, K. Anchouche, G. Singh, P.J. Slomka, K.K. Kolli, A. Kumar, et al. Clinical applications of machine learning in cardiovascular disease and its relevance to cardiac imaging, Eur. Heart J. 40 (24) (2019) 1975-1986. doi: 10.1093/eurheartj/ehy404

[34] X. Zhuang, L. Li, C. Payer, D. Stern, M. Urschler, M., M.P. Heinrich, et al. Evaluation of algorithms for multi-modality whole heart segmentation: an open-access grand challenge, Med. Image Anal. (2019) 101537 (In press). doi: 10.1016/j.media.2019.101537

[35] V. Zlokolica, L. Krstanović, L. Velicki, B. Popović, M. Janev, R. Obradović, N.M. Ralević, L. Jovanov, D. Babin, Semiautomatic epicardial fat segmentation based on fuzzy c-means clustering and geometric ellipse fitting, J. Healthc. Eng. 2017 (2017) 5817970. doi: 10.1155/2017/5817970

[36] C. Militello, S. Vitabile, L. Rundo, G. Russo, M. Midiri, M. C. Gilardi, A fully automatic 2D segmentation method for uterine fibroid in MRgFUS treatment evaluation, Comput. Biol. Med. 62 (2015) 277–292. doi: 10.1016/j.compbiomed.2015.04.030

[37] G. Coppini, R. Favilla, P. Marraccini, D. Moroni, G. Pieri, Quantification of epicardial fat by cardiac CT imaging, Open Med. Inform. J. 4 (2010) 126–135. doi: 10.2174/1874431101004010126

[38] X. Yang, H. Dou, R. Li, X. Wang, C. Bian, S. Li, D. Ni, P.A. Heng, Generalizing deep models for ultrasound image segmentation, in: Proc. International Conference on Medical Image Computing and Computer-Assisted Intervention (MICCAI), Springer, 2018, pp. 497–505. doi: 10.1007/978-3-030-00937-3_57

[39] L. Rundo, C. Han, Y. Nagano, J. Zhang, R. Hataya, R., Militello C., et al., USE-Net: incorporating Squeeze-and-Excitation blocks into U-Net for prostate zonal segmentation of multi-institutional MRI datasets, Neurocomputing. doi: 10.1016/j.neucom.2019.07.006 (In press)

[40] Y. Boykov, M.P. Jolly, Interactive organ segmentation using graph cuts, Proc. Medical Image Computing and Computer-Assisted Intervention (MICCAI) 2000. Lecture Notes in Computer Science, vol. 1935, Springer, Berlin, Heidelberg, Germany. doi: 10.1007/978-3-540-40899-4_28

[41] L. Rundo, C. Militello, G. Russo, S. Vitabile, M.C. Gilardi, G. Mauri, GTVcut for neuro-radiosurgery treatment planning: an MRI brain cancer seeded image segmentation method based on a cellular automata model, Nat. Comput. 17 (3) (2018) 521–536. doi: 10.1007/s11047-017-9636-z

[42] A. Hamamci, N. Kucuk, K. Karaman, K. Engin, G. Unal, Tumor-Cut: segmentation of brain tumors on contrast enhanced MR images for radiosurgery applications, IEEE Trans. Med. Imaging 31 (3) (2012) 790–804. doi: 10.1109/TMI.2011.2181857

[43] T. Yoshizumi, T. Nakamura, M. Yamane, A.H.M., Waliul Islam, M. Menju, M., K. Yamasaki, T. Arai, K. Kotani, T. Funahashi, S. Yamashita, Y. Matsuzawa, Abdominal fat: standardized technique for measurement at CT, Radiology 211 (1) (1999) 283–286. doi: 10.1148/radiology.211.1.r99ap15283

[44] F.E. Boas, D. Fleischmann, CT artifacts: causes and reduction techniques, Imaging Med. 4 (2) (2012) 229–240. doi: 10.2217/iim.12.13

[45] A.D. Villa, E. Sammut, A. Nair, R. Rajani, R. Bonamini, A. Chiribiri, Coronary artery anomalies overview: the normal and the abnormal, World J. Radiol. 8 (6) (2016) 537–555. doi: 10.4329/wjr.v8.i6.537

[46] O. Rickards, C. Martinez-Labarga, G. Scano, G.F. De Stefano, Genetic history of the population of Sicily, Hum. Biol. 70 (4) (1998) 699–714.

[47] S. Sarno, A. Boattini, L. Pagani, M. Sazzini, S. De Fanti, A. Quagliariello, et al., Ancient and recent admixture layers in Sicily and Southern Italy trace multiple migration routes along the Mediterranean, Sci. Rep. 7 (1) (2017) 1984. doi: 10.1038/s41598-017-01802-4

[48] M.J. Tapiovaara, R. Wagner SNR and DQE analysis of broad spectrum X-ray imaging. Phys. Med. Biol. 30 (6) (1985) 519-529. doi: 10.1088/0031-9155/30/6/002

[49] M.J. Firbank, A. Coulthard, R.M. Harrison, E.D. Williams, A comparison of two methods for measuring the signal to noise ratio on MR images. Phys. Med. Biol. 44 (12) (1999) N261. doi: 10.1088/0031-9155/44/12/403

[50] A.A. Taha, A. Hanbury, Metrics for evaluating 3D medical image segmentation: analysis, selection, and tool, BMC Med. Imaging 15 (1) (2015) 29. doi: 10.1186/s12880-015-0068-x

[51] F. Cabitza, R. Rasoini, G.F. Gensini, Unintended consequences of machine learning in medicine, JAMA 318 (6) (2017) 517–518. doi: 10.1001/jama.2017.7797

[52] O. Gambino, L. Rundo, V. Cannella, S. Vitabile, R. Pirrone, A framework for data-driven adaptive GUI generation based on DICOM, J. Biomed. Inform. 88 (2019) 37–52. doi: 10.1016/j.jbi.2018.10.009

[53] V.Y. Cheng, D. Dey, B. Tamarappoo, R. Nakazato, H. Gransar, R. Miranda-Peats, A. Ramesh, N. D. Wong, L.J. Shaw, P.J. Slomka, D.S. Bernam, Pericardial fat burden on ECG-gated noncontrast CT in asymptomatic patients who subsequently experience adverse cardiovascular events, JACC Cardiovasc. Imaging 3 (4) (2010) 352–360. doi: 10.1016/j.jcmg.2009.12.013

[54] C.X. Wong, H.S. Abed, P. Molaee, A.J. Nelson, A.G. Brooks, G. Sharma, D.P. Leong, D.H. Lau, M.E. Middeldorp, K.C. Roberts-Thomson, G.A. Wittert, W.P. Abhayaratna, S.G. Worthley, P. Sanders, Pericardial fat is associated with atrial fibrillation severity and ablation outcome, J. Am. Coll. Cardiol. 57 (17) (2011) 1745–1751. doi: 10.1016/j.jacc.2010.11.045

[55] S.N. Hatem, P. Sanders, Epicardial adipose tissue and atrial fibrillation, Cardiovasc. Res. 102 (2) (2014) 205–213. doi: 10.1093/cvr/cvu045

[56] T. Mazurek, M. Kiliszek, M. Kobylecka, J. Skubisz-Głuchowska, J. Kochman, K. Filipiak, L. Królicki, G. Opolski, Relation of proinflammatory activity of epicardial adipose tissue to the occurrence of atrial fibrillation, Am. J. Cardiol. 113 (9) (2014) 1505–1508. doi: 10.1016/j.amjcard.2014.02.005

[57] B.D. De Vos, J.M. Wolterink, P.A. De Jong, T. Leiner, M.A. Viergever, I. Isgum, ConvNet-based localization of anatomical structures in 3-D medical images, IEEE Trans. Med. Imaging 36 (7) (2017) 1470-1481. doi: 10.1109/TMI.2017.2673121

[58] G. Singh, S.J. Al'Aref, M. Van Assen, T.S. Kim, A. van Rosendael, K.K. Kolli, et al. Machine learning in cardiac CT: basic concepts and contemporary data, J. Cardiovasc. Comput. Tomogr. 12 (3) (2018) 192-201. doi: 10.1016/j.jcct.2018.04.010